



Faculty of Postgraduate studies and Scientific Research

German University in Cairo

**Magnetic-Based Motion Control of  
Sperm-Shaped Microrobots using  
Weak Oscillating Magnetic Fields**

by

Kareem Youakim

supervised by

Ass. Prof. Islam S. M. Khalil

co-supervised by

Prof. ELSayed Ibrahim Imam Morgan

and

Prof. Sarthak Misra

A thesis submitted in partial fulfillment for the  
degree of Masters of Science in Mechatronics Engineering

# Declaration of Authorship

I, Kareem Youakim, declare that this thesis titled, ‘Magnetic-Based Motion Control of Sperm-Shaped Microrobots using Weak oscillating Magnetic Fields’ and the work presented in it are my own. I confirm that:

- This work was done wholly or mainly while in candidature for a research degree at this University.
- Where any part of this thesis has previously been submitted for a degree or any other qualification at this University or any other institution, this has been clearly stated.
- Where I have consulted the published work of others, this is always clearly attributed.
- Where I have quoted from the work of others, the source is always given. With the exception of such quotations, this thesis is entirely my own work.
- I have acknowledged all main sources of help.
- Where the thesis is based on work done by myself jointly with others, I have made clear exactly what was done by others and what I have contributed myself.

Signed:

---

Date:

---



# Abstract

Microrobotics have the potential to be used in various medical applications. Targeted drug delivery can be accomplished by coating microrobots with drugs and controlling their motion to reach the specified diseased cells. However, the small size of magnetic microrobots ( $<500 \mu\text{m}$ ) causes difficulty in their locomotion due to the relatively large electromagnets needed to supply enough magnetic field gradient to pull them. This thesis proposes a locomotion mechanism based on driving microrobots using weak oscillating magnetic fields. First, a sperm-shaped microrobot which is referred to as MagnetoSperm consists of a magnetic head and a flexible tail. Weak oscillating magnetic fields (less than 5 mT) cause the head of the MagnetoSperm to oscillate, and hence induce a traveling wave along the flexible tail. The MagnetoSperm then propels forward. Closed-loop control using a closed electromagnetic system is applied on the MagnetoSperm while sliding on the surface of a petri-dish. MagnetoSperm with triangular and elliptical heads are used in the experiments where each MagnetoSperm slides toward 5 reference points at frequencies of 5 Hz and 45 Hz. The MagnetoSperm with the triangular head has a maximum velocity of  $15.09 \mu\text{m/s}$  at 45 Hz and a maximum velocity of  $60.55 \mu\text{m/s}$  at 5 Hz. The MagnetoSperm with the elliptical head has a maximum velocity of  $7.93 \mu\text{m/s}$  at 5 Hz and a maximum velocity of  $35.93 \mu\text{m/s}$  at 45 Hz. Second, this thesis shows the effect of applying oscillating magnetic fields on microparticles sliding on a surface. A decrease of 75 % in magnetic field is observed when oscillating magnetic fields are applied to pull the sliding microparticles. The characterization of sliding microparticles is done by applying a range of alternating frequencies from 5 Hz to 55 Hz. Clusters of 3 to 4 microparticles and clusters of 5 to 9 microparticles are used in these experiments. Clusters of 5 to 9 microparticles experience the highest average velocity of  $1500 \mu\text{m/s}$  at a frequency of 30 Hz. Point-to-point closed-loop control and trajectory control are also used to control the motion of the sliding microparticles. An average velocity of  $223 \mu\text{m/s}$  and a steady-state error of  $20 \mu\text{m}$  are measured in the point-to-point closed-loop experiment while an average velocity of  $60 \mu\text{m/s}$  is measured in controlling the sliding microparticles in a circular trajectory.

# Publications

- I. S. M. Khalil, K. Youakim, A. Sanchez, and S. Misra Magnetic-based motion control of sperm-shaped microrobots using weak oscillating magnetic fields, *IEEE International Conference of Robotics and Systems (IROS)*, pp. 4686-4691, Chicago, USA, September 2014.
- K. Youakim, M. Ehab, O. Hatem, S. Misra, and I. S. M. Khalil, "Paramagnetic microparticles sliding on a surface: characterization and closed-loop motion control." *IEEE International Conference of Robotics and Automation (ICRA)*, pp. 4068-4073, Seattle, USA, May 2015.

# Acknowledgements

First, I would like to thank my supervisor Dr. Islam S. M. Khalil for all his help and support. Also, I would like to thank Prof. Sarthak Misra and Dr. Alonso Sanchez for their help in the motion control of the MagnetoSperm. I would also like to thank Mr. Mohamed Ehab and Mr. Omar Hatem for their help in researching the effect of oscillating magnetic fields on sliding microparticles. Moreover, I would like to thank Mr. Bishoy Naguib for designing the electromagnetic setup.

# Contents

<b>Declaration of Authorship</b>	<b>i</b>
<b>Abstract</b>	<b>iii</b>
<b>Publications</b>	<b>iv</b>
<b>Acknowledgements</b>	<b>v</b>
<b>List of Figures</b>	<b>viii</b>
<b>List of Tables</b>	<b>xii</b>
<b>1 Introduction</b>	<b>1</b>
1.1 Biologically Inspired Microrobots . . . . .	2
1.2 Biological Nanorobots . . . . .	7
1.3 Chemically Driven Microrobots . . . . .	8
1.4 Thesis Overview . . . . .	11
<b>2 MagnetoSperm</b>	<b>13</b>
2.1 Fabrication of MagnetoSperm . . . . .	14
2.2 Modelling of MagnetoSperm . . . . .	15
2.3 Open-Loop Control of MagnetoSperm . . . . .	18
2.4 Closed-Loop Control of MagnetoSperm . . . . .	19
2.4.1 Experimental Results . . . . .	22
<b>3 Sliding Microparticles</b>	<b>31</b>
3.1 Modelling of the Sliding Microparticles . . . . .	32
3.2 Electromagnetic System . . . . .	35
3.3 Experimental Results . . . . .	35
3.3.1 Proof of Concept . . . . .	36
3.3.2 Frequency Response of Clusters of Microparticles . . . . .	36
3.3.3 Closed-Loop Control of the Cluster of Sliding Microparticles . . . . .	39

---

<b>4</b>	<b>Conclusions</b>	<b>46</b>
<b>A</b>	<b>Setup Design</b>	<b>48</b>
A.1	Base . . . . .	48
A.2	Holders . . . . .	49
A.3	Assembly . . . . .	49
<b>B</b>	<b>Microparticles Data Sheet</b>	<b>50</b>
	<b>Bibliography</b>	<b>52</b>

# List of Figures

1.1	Schematic representation of microrobots (MagnetoSperms) swimming in blood vessels. This schematic representation is designed using Blender (Blender 2.71, Blender Foundation, Entrepotdok, Amsterdam, The Netherlands). . . . .	2
1.2	Schemataic representation of an artificial flagella. The artificial flagella consists of magnetic particles ( $1 \mu\text{m}$ in diameter) attached together with DNA strands $107 \text{ nm}$ long. The streptavidin (red cross symbols) bond the particles with the DNA strands. A magnetic field $B_x$ is applied to impose a straight configuration to the filament. This schematic representation has been adapted from [8]. . . . .	3
1.3	Schematic representation of a helical magnetic microrobot. The microrobot has a magnetic head which rotates when a weak rotating magnetic field ( $B$ ) is applied. This rotation allows the microrobot to move forward. This schematic representation has been adapted from [12]. . . . .	5
1.4	A scanning Electron Microscopy image of glass propeller-like microrobot. The microrobot has a helical tail to allow forward propulsion when rotating magnetic fields are applied to it. The microrobots are $1$ to $2 \mu\text{m}$ long and $200$ to $300 \text{ nm}$ wide [13]. .	6
2.1	Image of a MagnetoSperm. The MagnetoSperm consists of a magnetic head and a flexible tail of $42 \mu\text{m}$ and $280\mu\text{m}$ , respectively. The MagnetoSperm also has a thickness, length and width of $5.2 \mu\text{m}$ , $322 \mu\text{m}$ and $42 \mu\text{m}$ . The magnetic head oscillates when the oscillating magnetic fields are applied to it. This allows the tail also to oscillate and propagate the MagnetoSperm forward [32]. . . . .	14
2.2	A schematic representation of the electromagnetic setup. Two opposite electromagnetic coils provide weak oscillating magnetic fields for propulsion, while the other two electromagnetic coils are provided with a current of $1 \text{ Ampere}$ to control the direction.	17

2.3	Open-loop motion control of MagnetoSperm. The oscillating fields are turned off at $t = 0, t = 4$ and $t = 7.6$ seconds where the MagnetoSperm does not move. The MagnetoSperm only swims when the weak oscillating magnetic fields are turned on at $t = 1.9, t = 5.5$ and $t = 10.8$ seconds. The swimming speed of the MagnetoSperm in this experiment is $107 \mu\text{m/s}$ and the frequency of the oscillating fields is $50 \text{ Hz}$ [32]. . . . .	18
2.4	Schematic representation of the closed-loop control. Electromagnets A, B, C, and D are used to control the motion of the MagnetoSperm. $e_x, e_y$ and $\theta$ are the errors in the $x$ axis and $y$ axis respectively and the direction of motion. The blue dot indicates the reference position (a) Electromagnets A and B are supplied with uniform currents to control the direction of the MagnetoSperm while electromagnets C and D are supplied with alternating currents to oscillate the head of the MagnetoSperm. (b) Electromagnets C and D are supplied with uniform currents to direct the MagnetoSperm towards the reference position while electromagnets A and B produce alternating magnetic fields.	21
2.5	Swimming and sliding speeds of MagnetoSperm at $5 \text{ Hz}$ and $45 \text{ Hz}$ . The swimming speeds are calculated using open-loop control trails while sliding speeds are calculated using closed-loop control trails. The MagnetoSperm swims while fully immersed in water and slides while in contact with the bottom. . . . .	27
2.6	Point-to-Point closed-loop control of the MagnetoSperm at $5 \text{ Hz}$ . (a) The MagnetoSperm slides on the bottom of the petri-dish to reach its reference position. A feature tracking algorithm is used to track the MagnetoSperm and control its motion. (b) Graphical plot of the point-to-point motion control of the MagnetoSperm. . . . .	29
2.7	Point-to-Point closed-loop control of the MagnetoSperm at $45 \text{ Hz}$ . (a) The MagnetoSperm slides on the bottom of the petri-dish to reach its reference position. A feature tracking algorithm is used to track the MagnetoSperm and control its motion. (b) Graphical plot of the point-to-point motion control of the MagnetoSperm. . . . .	30
3.1	Schematic representation of microparticles sliding on the lumen of blood veins. The white arrows represent the magnetic field oscillations which allow the microparticles to overcome the static friction. The microparticles are pulled by the weak magnetic field gradients represented by blue arrows. Experiments are done using clusters of microparticles (as seen in the inset on the top-left corner) using the electromagnetic setup shown in the bottom-right corner. This schematic representation is designed using Blender (Blender 2.71, Blender Foundation, Entrepotdok, Amsterdam, The Netherlands). . . . .	32

3.2	Schematic representation showing the modelling of the sliding microparticles. The green arrow indicates the friction force. The blue arrow indicates the drag force while the red arrow indicates the magnetic force. The magnetic force is larger when oscillating magnetic fields are not applied. (a) The forces exerted on the sliding microparticles without oscillating fields. (b) The forces exerted on the sliding microparticles with oscillating microparticles. . . . .	33
3.3	Electromagnetic setup used for the characterization and control of the microparticles. The setup consists of an orthogonal array of electromagnets to produce the oscillating magnetic fields in order to overcome the static friction and the magnetic field gradient to pull the particles. An optical microscope is used to track the motion of the particles. The bottom-left inset shows a cluster of 9 particles oscillating due to the alternating magnetic fields represented by the white arrows. The red arrow represents the direction of motion of the particles. . . . .	34
3.4	A constant magnetic field are applied to a cluster of 3 microparticles throughout the experiment. Alternating magnetic fields are turned on and off over the length of the experiment. The red arrow represents the constant field while the the white arrow represents the alternating fields. The alternating fields are applied after $t = 1.5$ seconds, $t = 4.5$ seconds and $t = 6.7$ seconds. The microparticles overcome the static friction and slide at a velocity of $300 \mu\text{m/s}$ at a frequency of 30 Hz. . . . .	37
3.5	Frequency response of clusters of sliding microparticles. Clusters of 3 to 4 and 5 to 9 microparticles are used in the experiments. The average velocity of 5 trials is calculated at each frequency. The clusters have zero speed when no oscillation are applied. A constant gradient of 0.9 T/m is applied through all the experiments. . . . .	38
3.7	Microparticles sliding on the surface of a petri-dish at a oscillating frequency of 40 Hz and an average speed of 3 body lengths per second. The white arrows indicate the oscillating magnetic fields while the blue and red dashed lines indicate the start and ending positions of the microparticles. . . . .	40
3.6	The minimum magnetic field required to pull the microparticles. The magnetic field gradient is increased gradually at a frequency of 0 Hz until the microparticles move at a magnitude of 13.4 mT. The experiment is repeated for frequencies from 5 Hz to 50 Hz and the average magnitude of the magnetic field gradient is measured to be 3.37 mT. This gives a 75% decrease in the magnetic field gradient needed to pull the microparticles when magnetic field oscillations are applied. . . . .	40

- 
- 3.8 Schematic representation of the closed-loop control. Electromagnets A, B, C, and D are used to control the motion of the Microparticles.  $e_x$ ,  $e_y$  and  $\theta$  are the errors in the  $x$  axis and  $y$  axis respectively and the direction of motion. The blue dot indicates the reference position (a) Electromagnets A and B are supplied with uniform currents to control the direction of the Microparticles while electromagnets C and D are supplied with alternating currents to oscillate the head of the Microparticles. (b) Electromagnets C and D are supplied with uniform currents to direct the Microparticles towards the reference position while electromagnets A and B produce alternating magnetic fields. . . . . 42
- 3.9 Closed-loop control of sliding microparticles. a) The microparticles slide toward 3 different reference positions. The average speed calculated is  $223 \mu\text{m/s}$  and the maximum steady-state error is  $20 \mu\text{m}$ . b) The red vertical lines represent the reference positions (which are represented by the small white squares in the snap-shots). The blue lines indicate the trajectory of the microparticles. . . . . 43
- 3.10 Closed-loop control of sliding microparticles in a circular trajectory. a) 20 reference positions identify circular trajectory with a diameter of  $1904 \mu\text{m}$ . The average velocity of the microparticles is  $60 \mu\text{m/s}$ . b) The blue line indicates the path of the microparticles and the dashed-red circle indicates the reference circular trajectory. The direction of the cluster and the position of the cluster are indicated by the black arrows and the white squares respectively. . . . . 44

# List of Tables

- 2.1 Point-to-point control of MagnetoSperm with triangular head at a frequency of 45 Hz.  $\mathbf{V}_x$ ,  $\mathbf{V}_y$  and  $\mathbf{V}_r$  are the velocities in the  $x$ -axis,  $y$ -axis and resultant velocity respectively, while  $\mathbf{ROC}_x$ ,  $\mathbf{ROC}_y$  and  $\mathbf{ROC}_r$  are the region of convergence in the  $x$ -axis,  $y$ -axis and resultant region of convergence respectively. Experiments are done at 5 different points. The MagnetoSperm has a length of  $322 \mu\text{m}$  and the magnetic field applied is about 5 mT. . . . . 22
- 2.2 Point-to-point control of MagnetoSperm with triangular head at a frequency of 5 Hz.  $\mathbf{V}_x$ ,  $\mathbf{V}_y$  and  $\mathbf{V}_r$  are the velocities in the  $x$ -axis,  $y$ -axis and resultant velocity respectively, while  $\mathbf{ROC}_x$ ,  $\mathbf{ROC}_y$  and  $\mathbf{ROC}_r$  are the region of convergence in the  $x$ -axis,  $y$ -axis and resultant region of convergence respectively. Experiments are done at 5 different points. The MagnetoSperm has a length of  $322 \mu\text{m}$  and the magnetic field applied is about 5 mT. 24
- 2.3 Point-to-point control of MagnetoSperm with elliptical head at a frequency of 45 Hz.  $\mathbf{V}_x$ ,  $\mathbf{V}_y$  and  $\mathbf{V}_r$  are the velocities in the  $x$ -axis,  $y$ -axis and resultant velocity respectively, while  $\mathbf{ROC}_x$ ,  $\mathbf{ROC}_y$  and  $\mathbf{ROC}_r$  are the region of convergence in the  $x$ -axis,  $y$ -axis and resultant region of convergence respectively. Experiments are done at 5 different points. The MagnetoSperm has a length of  $322 \mu\text{m}$  and the magnetic field applied is about 5 mT. 25
- 2.4 Point-to-point control of MagnetoSperm with elliptical head at a frequency of 5 Hz.  $\mathbf{V}_x$ ,  $\mathbf{V}_y$  and  $\mathbf{V}_r$  are the velocities in the  $x$ -axis,  $y$ -axis and resultant velocity respectively, while  $\mathbf{ROC}_x$ ,  $\mathbf{ROC}_y$  and  $\mathbf{ROC}_r$  are the region of convergence in the  $x$ -axis,  $y$ -axis and resultant region of convergence respectively. Experiments are done at 5 different points. The MagnetoSperm has a length of  $322 \mu\text{m}$  and the magnetic field applied is about 5 mT. 26

*I dedicate this first and foremost to my God for giving me the strength to go on. To my parents and brother for the love they always give me and to my friends for their continuous support.*



# Chapter 1

## Introduction

Nowadays, much attention is being directed towards research in microrobotic and nanorobotic systems [1–33, 37–40] due to their importance in medical applications. There are increasing demands for minimal invasive surgery for treatment and diagnosis. These demands could be met by microrobotic systems. Microrobots can be controlled and steered inside blood vessels to reach specific destinations. One of their main applications is targeted drug delivery where microrobots could be coated with drugs and navigated to reach specific diseased cells inside the human body as seen in Figure 1.1. Another application is to direct small surgical needles on the retina of the eye to perform minimal invasive surgeries [1]. Microrobots also have potential for non-medical applications such as microassembly of microsystems and micromanipulation of microscale objects [2]. Different propulsion mechanisms have been investigated by researchers. Examples for propulsion systems include bubble propulsion [3], electrical propulsion [4], ultrasound propulsion [5] and magnetic propulsion [6].

One way to drive microrobots is by pulling them using the gradient of the field [7]. The problem in this approach is that the gradient of the magnetic field has smaller projection distance than the projection distance of the magnetic field. This property decreases the practicality as one would have to scale up the electromagnetic system in order to perform *in vivo* applications. Therefore, other propulsion techniques are investigated where the magnetic field is only used to steer the microrobot.

## 1.1 Biologically Inspired Microrobots

The first proposed microrobot is inspired by *eukaryotic* flagella [8]. These elastic rod-like flagella exhibit a beating motion which leads to their forward

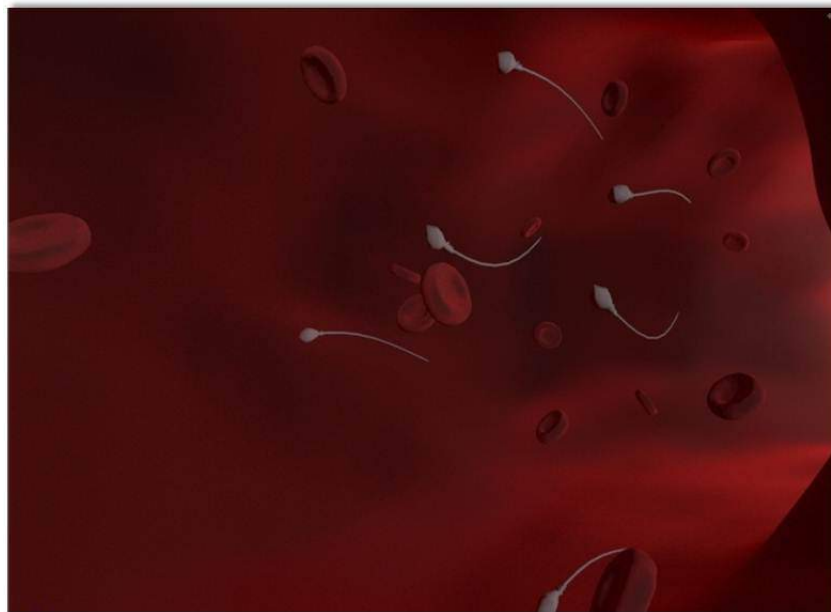


FIGURE 1.1: Schematic representation of microrobots (MagnetoSperms) swimming in blood vessels. This schematic representation is designed using Blender (Blender 2.71, Blender Foundation, Entrepotdok, Amsterdam, The Netherlands).

motion. The artificial flagella is made of a series of colloidal magnetic particles attached together with short flexible DNA joints. A varying magnetic field is produced to transfer energy into the artificial flagella. The flagella is used to push and transport a red blood cell. The size of each superparamagnetic colloid is  $1 \mu\text{m}$  in diameter, and the DNA have lengths of  $107 \text{ nm}$ . A schematic representation is provided in Figure 1.2. Varying magnetic fields are also applied on a rectangular shaped microrobot to produce a stick-slip motion [9, 10]. This microrobot is fabricated using a neodymium-iron-boron permanent magnet with dimensions of  $250 \mu\text{m} \times 130 \mu\text{m} \times 10 \mu\text{m}$ . A system of six electromagnets is used to provide the magnetic torque necessary to propel the microrobot. An out-of-plane pulsing method is mainly used where the magnetic field within the plane of motion is kept constant while the magnetic field perpendicular to the plane of motion is varied. This produces a clamping motion which allows the microrobot to move forward. The translational speed of the microrobots observed to be higher than  $10 \text{ mm/s}$ . Another robot which

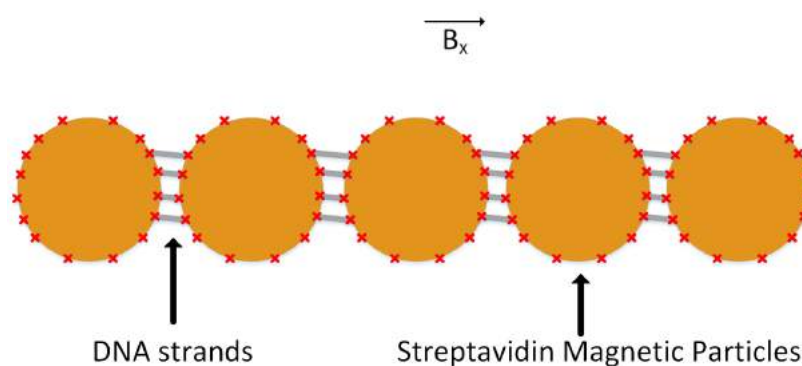


FIGURE 1.2: Schematic representation of an artificial flagella. The artificial flagella consists of magnetic particles ( $1 \mu\text{m}$  in diameter) attached together with DNA strands  $107 \text{ nm}$  long. The streptavidin (red cross symbols) bond the particles with the DNA strands. A magnetic field  $B_x$  is applied to impose a straight configuration to the filament. This schematic representation has been adapted from [8].

---

moves using stick-slip motion is used to manipulate cells [11]. The microrobot is composed of iron oxide nanoparticles embedded in SU-8 with a size of  $30 \mu\text{m} \times 30 \mu\text{m} \times 10 \mu\text{m}$ . A setup with 5 electromagnetic coils is used to control the motion of the microrobot. First, the microrobots sort the microbeads into 3 different piles according to their size. Then, the microrobots position individual microbeads in specific locations. A mouse embryo of  $15 \mu\text{m}$  in diameter is autonomously positioned using the microrobot. The microrobot also transports yeast and neurons to different locations. Polymeric microbeads are doped with chemicals and transported using the microrobot. This shows the capability of carrying drugs to targeted diseased cells. Microrobots mimicking microorganisms with helical flagella have also been produced [12]. Magnetic helical microrobots depend on rotating magnetic fields for their propulsion. The weak rotating magnetic fields rotate the magnetic helical microrobots. The microrobots rotate because their magnetic dipole moment continuously aligns itself with the rotating magnetic field. This rotation produces a propulsion force which allows the microrobot to swim forward. This microrobot has an average length of  $40 \mu\text{m}$ . A schematic representation of this robot can be seen in Figure 1.3

Propeller-like microrobots are also produced from glass ( $\text{SiO}_2$ ) [13]. These glass fabricated helical structures are  $1 \mu\text{m}$  to  $2 \mu\text{m}$  long and 200 to 300 nm wide. After they are fabricated, a thin cobalt layer (30 nm) is deposited using thermal evaporation onto their surface. The microrobots are then placed between the pole pieces of an electromagnet to magnetize the cobalt. Rotating magnetic fields up to 170 Hz are produced using a triaxial Helmholtz coil.

The magnetic moment of the microrobot couples with the rotating magnetic field of the coil causing the microrobot to rotate around its body axis. The microrobot translates forward or backward after each rotation. A velocity of approximately  $40 \mu\text{m/s}$  is observed at a rotating frequency of 150 Hz. The helical microrobots are controlled in a trajectory and are used to push a silica bead of  $5 \mu\text{m}$  diameter. An image of the microrobot can be seen in Figure 1.4.

Research has also led to the development of microrobots with multiple flexible flagella [14]. A sub-millimeter scale robot consists of a cylindrical body made of a permanent magnetic based composite (NeodymiumIronBoron and polyurethane). Artificial flexible flagella are attached to the magnetic body. When rotating magnetic fields are applied, the magnetic body rotates and conveys this rotation to the artificial flagella. The flagella then bends into chiral shapes because of viscous drag which results in a net axial force to propel the microrobot forward. Microrobots are produced with different sizes ranging from  $500 \mu\text{m}$  to  $180 \mu\text{m}$  of body length. The artificial flagella is also produced between 1.5 mm and 1 mm in length. A rotating magnetic field of 12 mT is

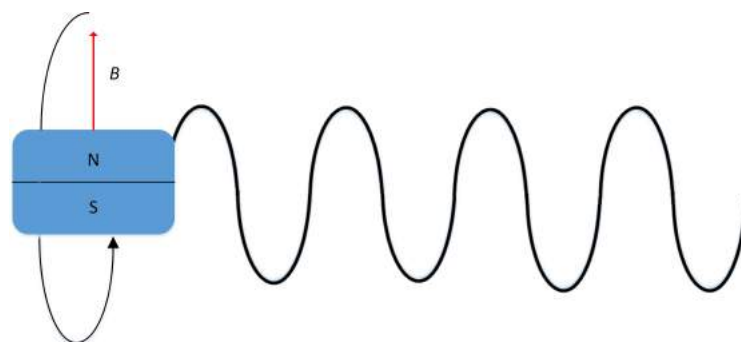


FIGURE 1.3: Schematic representation of a helical magnetic microrobot. The microrobot has a magnetic head which rotates when a weak rotating magnetic field ( $B$ ) is applied. This rotation allows the microrobot to move forward. This schematic representation has been adapted from [12].

used during the experiment. The results showed that increasing the number of flagella from 1 to 4 linearly increased the speed of the microrobot. However, when the number of flagella increased from 4 to 6, the speed of the microrobot decreased due to small spaces between the flagella which leads to a smaller propulsive force generated by each flagella. The microrobot reached a maximum speed of 0.4 mm/s when a rotating frequency of 12 Hz is applied to a microrobot with a body length of 180  $\mu\text{m}$  and a flagella length of 1 mm. Independent control of multiple magnetic microrobots using the same closed-loop configuration has also been investigated [15].

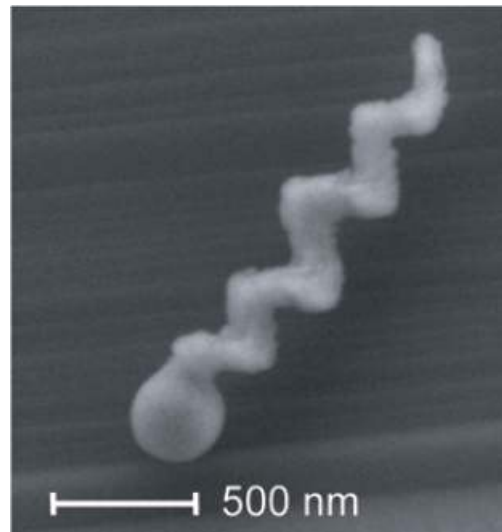


FIGURE 1.4: A scanning Electron Microscopy image of glass propeller-like microrobot. The microrobot has a helical tail to allow forward propulsion when rotating magnetic fields are applied to it. The microrobots are 1 to 2  $\mu\text{m}$  long and 200 to 300 nm wide [13].

---

## 1.2 Biological Nanorobots

Another approach used in nanorobotics is using biological organisms as nanorobots instead of developing artificial nanorobots [2, 16, 17]. This is achieved by controlling magnetotactic bacteria. This strand of bacteria has magnetic properties which allow them to be steered using magnetic fields. The magnetotactic bacteria have diameters ranging from 1 to 2  $\mu\text{m}$  and can reach velocities of 200 to 300  $\mu\text{m/s}$ . The bacteria are naturally propelled using their own flagella and are steered using an electromagnetic system. Swarms of this bacteria is used in microassembly to assemble a small pyramid with building blocks of 80  $\mu\text{m} \times 20 \mu\text{m} \times 15 \mu\text{m}$ . Position control has also been done on a single magnetotactic bacterium [18]. Due to the small size of the bacterium, its dipole moment has an order of magnitude which ranges from  $10^{-18}$  to  $10^{-16}$  A/m<sup>2</sup>. This requires relatively very large magnetic fields in order to stop the magnetotactic bacteria at a reference position. Therefore, a null-space control system is proposed to decrease the position error of the magnetotactic bacterium. The speed of the magnetotactic bacterium decreased by 37% when an alternating field with a frequency of 85 Hz was applied. The region of convergence produced by the null-space controller is 15% smaller in comparison with a PD controller using the same gains. The results show that by increasing the frequency of the null-space input by 1 Hz, the position accuracy is enhanced by decreasing the region of convergence of the magnetotactic bacterium by approximately 10%. Researchers have also used bacteria which are not magnetic [19]. Flagellated bacteria is attached to a buoyancy-neutral plate called a microbarge (50  $\mu\text{m} \times 100 \mu\text{m}$ ). The distribution of the bacteria on the plate and the stimuli from the

environment causes the motion of the plate. A stochastic mathematical model of the system is constructed depending on the theory that each bacterium has a behavior which is independent of the other bacteria. The complex dynamics of the system is reduced to a system of three ordinary differential equations with only three parameters. The predictions from the theoretical model match the results of the experiments where the motion of the microbarge is tracked using a feature tracking program. Magnetic resonance imaging is also used to provide feedback for the motion control of biological nanorobots [20].

Sakar *et al.* have experimented on using MicroBioRobots (MBRs) [21]. SU-8 microstructures are blotted with motile bacteria of the strand *Serratia Marcescens*. The MBRs are propelled using the bacteria which are deposited on it. Self-actuation is done where no external stimuli are applied to the MBRs and they are solely actuated by the random motion of the bacteria. Closed-loop control is also done by applying DC voltages using electrodes to control the direction of motion of the bacteria since they carry charges. A microscope with a feature tracking algorithm to track the motion of the MBRs is also used. A  $20\ \mu\text{m} \times 22\ \mu\text{m}$  rectangular MBR is controlled in star-shaped, circular and diamond shaped paths.

### 1.3 Chemically Driven Microrobots

Chemical actuation is also used in the field of microrobotics [22–31]. Catalytic microjet engines are formed from rolled-up microtubes with inner catalytic

---

surfaces. A chemical reaction is formed between the surface and the surrounding fuel (an  $\text{H}_2\text{O}_2$  solution) causing bubbles to be produced and hence propelling the microtubes forward. The radius of the bubbles produced are proved to be inversely proportional with the frequency of the bubbles [22]. Also, larger bubbles cause a longer projection distance. The microtubes are 100  $\mu\text{m}$  long and 5.5  $\mu\text{m}$  in diameter. They propel forward with a speed of 2 mm/s and their motion can be controlled using magnetic fields if a ferromagnetic layer is incorporated into the tube. The microtubes are controlled in circular motions using rotating magnetic fields and are visualized by tracking the long microbubble tails. Microtubes are also used to transport and assemble micro-objects [23]. Titanium/Iron/Platinum films are rolled-up using nanotechnology to make microtubes 5  $\mu\text{m}$  in diameter and 50  $\mu\text{m}$  in length. An external small (10 mm  $\times$  7 mm  $\times$  5 mm ) permanent magnet is held by an actuator and placed beneath the microtubes. The magnet is left stationary if a straight motion of the microtubes is desired. The microtubes align themselves and change their direction with the magnetic field as it rotates. Polystyrene microparticles (5  $\mu\text{m}$  in diameter) are suspended in a fluid and pushed by the microtubes to deliver them to specific locations. The permanent magnetic slowly rotates until the microtube points toward the microparticles, the trajectory is then kept in a straight line until the microtube picks up the particles. As the number of microparticles increases from 0 to 60, the speed of the microtubes decreases from 80  $\mu\text{m/s}$  to 18  $\mu\text{m/s}$ . The microtubes also transport and assemble small nanoplates (25 nm thick and 50  $\mu\text{m}$  wide). The microtubes are filled with oxygen to increase their buoyancy and float them

---

to the surface where the plates are. Different assembly configurations of 1 to 4 nanoplates are accomplished. An inverse exponential behaviour is recorded between the speed of the microtubes and the surface area of the nanoplates. Titanium/iron/platinum microtubes are also self-propelled in microchannels of a microfluidics system [24]. A magnet is held by a stepper motor and positioned underneath the setup. A joystick controls the stepper motor to change the direction of the microtubes' motion. The microtubes are propelled against the flow and their speed drops from  $50 \mu\text{m/s}$  to  $30 \mu\text{m/s}$  when the flow rate increases from  $80 \mu\text{m/s}$  to  $100 \mu\text{m/s}$  in the opposite direction. Moreover, the speed of the microrobots increase from  $140 \mu\text{m/s}$  to  $180 \mu\text{m/s}$  when the flow is accelerated in the same direction. Microparticles with diameters of  $5 \mu\text{m}$  are also loaded onto the the microtubes. the microtube swims at a speed of  $160 \mu\text{m/s}$  when it is not loaded with microparticles and its speed decreases linearly when the microparticles are loaded. The speed of the microtube is  $125 \mu\text{m/s}$  when transporting 1 microparticle and decreases to  $72 \mu\text{m/s}$  when transporting 3 microparticles. Nanoscale rotors are also produced and propelled using chemical actuation [29]. Barcoded bimetal nanorods are developed with one segment made up of nickle and is used as a catalyst for the decomposition of  $\text{H}_2\text{O}_2$  where oxygen is produced to thrust the nanorod forward. The second segment is made out of a material which is non reactant to  $\text{H}_2\text{O}_2$  and in this case gold. The nanorods exhibit two main motions. Those which do not hold on to a silicon substrate migrate along the direction of the flow. When the gold end becomes anchored to the silicon substrate, the nanorod rotates in a way that resembles the hand of a clock. Self-propelled nanotools are produced

by depositing thin films of indium gallium arsenide and gallium arsenide on a gallium arsenide substrate [30]. The strain in the layers causes them to roll up into tubes with nanoscale diameters upon release from the substrate. A platinum layer is also deposited to make the tubes catalytically active in order for them to self-propel when put in  $\text{H}_2\text{O}_2$ . These self-propelled nanotubes have diameters which range from 280 nm -600 nm and reach speeds up to 180  $\mu\text{m/s}$ . Cylindrical nanotubes translate in a straight line while asymmetrical nanotubes move in a corkscrew-like trajectory which allow them to drill into biomaterials. These nanotubes are also used to transport multiple yeast cells to specific targets. Chemically driven nanorobots are also formed of nanorods instead of nanotubes [31]. Nanorods that are 370 nm in diameter are composed of platinum and gold where each segment is 1  $\mu\text{m}$  long. Platinum acts as an active  $\text{H}_2\text{O}_2$  decomposition catalyst while gold is not. The platinum reacts with the  $\text{H}_2\text{O}_2$  to produce a driving force to overcome the drag force of the fluid. The average speed of the nanorods is 8  $\mu\text{m/s}$  which is close to that of mutliflagellar bacteria.

## 1.4 Thesis Overview

This thesis proposes a new method to propel microrobots using sperm shaped microrobots called MagnetoSperms. MagnetoSperms have magnetic heads and flexible tails. The magnetic head of MagnetoSperm oscillates when weak oscillating magnetic fields are applied. These oscillations allow the tail also to

oscillate which leads to the forward propulsion of the MagnetoSperm. Chapter 2 introduces the control mechanism by which the MagnetoSperm is driven. The MagnetoSperm is controlled using an orthogonal array of electromagnets where two electromagnets produce weak alternating magnetic fields and the other two electromagnets produce uniform fields to direct the motion of the MagnetoSperm. Closed-loop motion control is done on sliding MagnetoSperms while in contact with the bottom of the petri-dish. In Chapter 3, experiments on applying oscillating magnetic fields to sliding microparticles are done to characterize their motion. Using a similar electromagnetic setup, the velocities of sliding microparticles are recorded against the frequency change of the oscillating magnetic fields and the number of particles used in a cluster. The experiments show that applying alternating magnetic fields makes it easier for the gradient of the magnetic field to pull the microparticles. Finally, a conclusion and discussion of the work is provided in Chapter 4.

## Chapter 2

# MagnetoSperm

The microrobot investigated in this thesis mimics the actuation method of human sperms. Human sperms have flexible tails which drive the sperms forward and allow them to swim. Similarly, this microrobot, which is called MagnetoSperm, has a magnetic head and a flexible tail as seen in Figure 2.1 . When alternating magnetic fields are applied, the head of the MagnetoSperm oscillates to orient itself with the magnetic fields. Accordingly, the tail of the MagnetoSperm also oscillates leading to its forward propulsion. This chapter discusses the fabrication of the MagnetoSperm, modelling of the MagnetoSperm and the motion control of the MagnetoSperm.

## 2.1 Fabrication of MagnetoSperm

The MagnetoSperm is fabricated in two steps [32]. First the main body is developed (head, neck and tail) then the magnetic material ( $\text{Co}_{80}\text{Ni}_{20}$ ) is deposited on the head. Material stability is achieved by selecting SU-8 as the structural material for the main body. SU-8-5 is first used to spin-coat a silicon wafer with  $\langle 100 \rangle$  crystal orientation and thickness and diameter of  $500 \mu\text{m}$  and  $100 \mu\text{m}$ , respectively. Ultraviolet exposure is used to transfer the MagnetoSperm patterns to the SU-8 after the pre-bake of the wafer. The SU-8 layer is developed in RER600 (ARCH Chemicals, Basel, Switzerland) to realize the MagnetoSperm bodies. Next, the wafer is hard baked to achieve material stability. The  $\text{Co}_{80}\text{Ni}_{20}$  is deposited on the head of the MagnetoSperm through a lift-off process. The wafer is spin-coated a  $10 \mu\text{m}$ -thick photoresist (AZ 9260) to transfer the layout of the magnetic material. The adhesion of the metal layer to the SU-8 is enhanced by a 30 seconds oxygen plasma treatment then a  $200 \text{ nm}$ -thick cobalt-nickel layer is deposited by e-beam evaporation and



FIGURE 2.1: Image of a MagnetoSperm. The MagnetoSperm consists of a magnetic head and a flexible tail of  $42 \mu\text{m}$  and  $280 \mu\text{m}$ , respectively. The MagnetoSperm also has a thickness, length and width of  $5.2 \mu\text{m}$ ,  $322 \mu\text{m}$  and  $42 \mu\text{m}$ . The magnetic head oscillates when the oscillating magnetic fields are applied to it. This allows the tail also to oscillate and propagate the MagnetoSperm forward [32].

lifted-off in acetone. The SU-8 is then made hydrophilic by another 30 seconds of Oxygen plasma treatment. Finally, the silicon wafer is etched away in a 5% Tetramethylammonium hydroxide (TMAH) solution at 85°C to release the MagnetoSperm.

## 2.2 Modelling of MagnetoSperm

As only the head of the MagnetoSperm is magnetic, it experiences a magnetic force ( $\mathbf{F}(\mathbf{P}) \in \mathbb{R}^{3 \times 1}$ ) and torque ( $\mathbf{T}(\mathbf{P}) \in \mathbb{R}^{3 \times 1}$ ) located at a position ( $\mathbf{P} \in \mathbb{R}^{3 \times 1}$ ) given by [34], [35]

$$\mathbf{F}(\mathbf{P}) = (\mathbf{m} \cdot \nabla)\mathbf{B}(\mathbf{P}) \quad \text{and} \quad \mathbf{T}(\mathbf{P}) = (\mathbf{m} \times \mathbf{B}(\mathbf{P})), \quad (2.1)$$

where  $\mathbf{m} \in \mathbb{R}^{3 \times 1}$  and  $\mathbf{B}(\mathbf{P}) \in \mathbb{R}^{3 \times 1}$  are the magnetic dipole moment of MagnetoSperm and the induced magnetic field, respectively. The drag force can be approximated by neglecting the head of MagnetoSperm and modelling it as a long thin needle of length  $l$  and diameter  $d$  [36]:

$$\mathbf{F}_d(\dot{\mathbf{P}}) = \eta \frac{l}{\ln(\frac{2l}{d}) - 0.81} \dot{\mathbf{P}}, \quad (2.2)$$

where  $\mathbf{F}_d(\dot{\mathbf{P}}) \in \mathbb{R}^{3 \times 1}$  and  $\dot{\mathbf{P}} \in \mathbb{R}^{3 \times 1}$  are the drag force and the velocity of the MagnetoSperm, respectively. Also,  $l$  and  $d$  are the length (322  $\mu\text{m}$ ) and diameter (5.2  $\mu\text{m}$ ) of MagnetoSperm, and  $\eta$  is the dynamic viscosity of water (1 mPa.s). The linear drag force is calculated using equation (2.2) to be  $1.2 \times 10^{-11}$  N at a speed of 158  $\mu\text{m/s}$  (maximum average speed of MagnetoSperm

at a frequency of 45 Hz). The magnetic dipole moment of MagnetoSperm experiences a magnetic force of

$$\mathbf{F}(\mathbf{P}) = \int_v M_s dv \cdot \nabla \mathbf{B}(\mathbf{P}) = \mathbf{m} \cdot \nabla \mathbf{B}(\mathbf{P}), \quad (2.3)$$

where  $\mathbf{F}(\mathbf{P})$  is the magnetic force at point  $(\mathbf{P})$ . Moreover,  $M_s$  is the magnetic saturation ( $1.19 \times 10^6$  A/m) and  $v$  is the volume of the  $\text{Co}_{80}\text{Ni}_{20}$  that is deposited on the head of the MagnetoSperm. At a magnetic field gradient of 2 mT/m, the maximum magnetic force exerted on the MagnetoSperm is calculated using equation (2.3) to be  $3.89 \times 10^{-13}$  N. This proves that the drag force is 2 orders-of-magnitude larger than the maximum magnetic force exerted by the magnetic system. Therefore, this shows that the motion of MagnetoSperm is due to the weak oscillating magnetic fields. In the case that MagnetoSperm slides on the surface of a blood vessel the equation of motion of the MagnetoSperm is given by

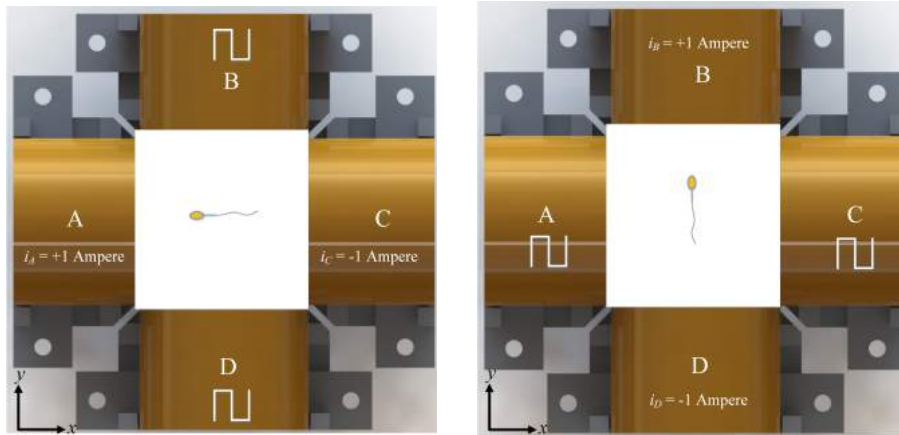
$$\mathbf{F}(\mathbf{P}) + \mathbf{F}_d(\dot{\mathbf{P}}) + \mathbf{F}_t + \mu_s \mathbf{R} = 0, \quad (2.4)$$

where  $\mathbf{F}_t$ ,  $\mu_s$  and  $\mathbf{R}$  are the propulsion force generated by the flexible tail due to the oscillating magnetic fields, the static coefficient of friction between the MagnetoSperm and a surface, and the reaction force on the MagnetoSperm, respectively. The force  $\mathbf{F}(\mathbf{P})$  in equation (2.4) is not enough to pull the Magnetosperm towards the reference but it contributes with the propulsion force generated from the oscillations of the Magnetosperm. The rotational dynamics of the MagnetoSperm constitutes of the magnetic torque, the torque produced

from the fluid drag and the torque due to the surface friction, this is given to be

$$|\mathbf{B}(\mathbf{P})||\mathbf{m}| \sin \phi + \alpha \dot{\theta} + \mu_s \mathbf{R}l = 0, \quad (2.5)$$

where  $\phi$  is the angle between the induced magnetic field and the magnetic dipole moment of the MagnetoSperm. Also,  $\alpha$  and  $\dot{\theta}$  are the rotational drag coefficient and the angular velocity of the MagnetoSperm, respectively. This shows that the magnetic torque must overcome the rotational drag and the frictional torque. If the angle between the magnetic field and the magnetic dipole moment is  $90^\circ$ , the magnetic torque exerted by the magnetic dipole moment of the MagnetoSperm will be maximum.



(a) MagnetoSperm swimming along  $x$ -axis (b) MagnetoSperm swimming along  $y$ -axis

FIGURE 2.2: A schematic representation of the electromagnetic setup. Two opposite electromagnetic coils provide weak oscillating magnetic fields for propulsion, while the other two electromagnetic coils are provided with a current of 1 Ampere to control the direction.

## 2.3 Open-Loop Control of MagnetoSperm

The electromagnetic system used in these experiments is a small scale version of the 5-DOF electromagnetic system called OctMag [1, 37]. This version consists of 4 orthogonal electromagnets. Each electromagnet has an inner-diameter, outer diameter, length and wire diameter of 10 mm, 40 mm, 30 mm, and 0.65 mm, respectively. This electromagnetic setup produces a magnetic field and gradient of 15 mT and 5 mT/m, respectively. Two electromagnets produce a weak sinusoidal field which allow the head of the MagnetoSperm to oscillate. As the head of the MagnetoSperm oscillates, its tail also oscillates leading to its forward propagation. The other two electromagnets provide a weak uniform field to control the direction of the MagnetoSperm. Controlling the MagnetoSperm this way only allows the MagnetoSperm to move in the four primary directions in the  $x$  and  $y$  axes as seen in Figure 2.2. Previous

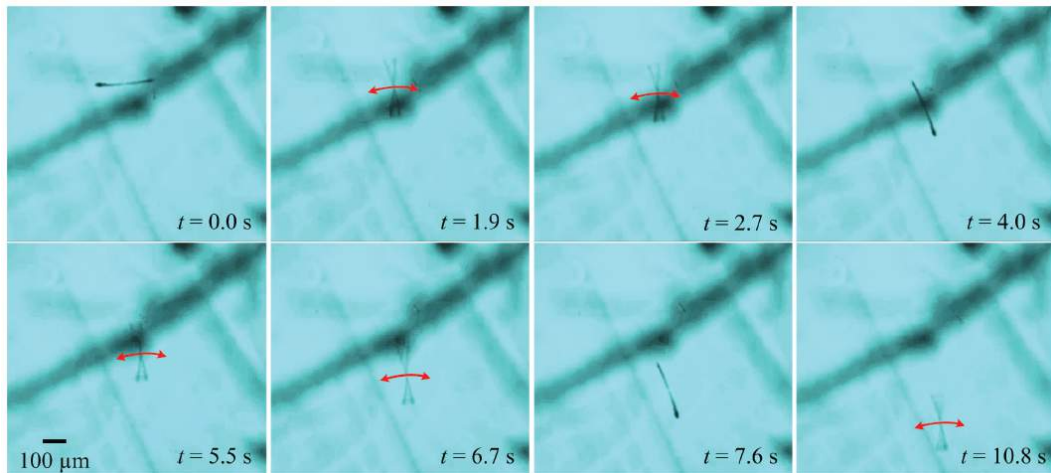


FIGURE 2.3: Open-loop motion control of MagnetoSperm. The oscillating fields are turned off at  $t = 0, t = 4$  and  $t = 7.6$  seconds where the MagnetoSperm does not move. The MagnetoSperm only swims when the weak oscillating magnetic fields are turned on at  $t = 1.9, t = 5.5$  and  $t = 10.8$  seconds. The swimming speed of the MagnetoSperm in this experiment is  $107 \mu\text{m/s}$  and the frequency of the oscillating fields is 50 Hz [32].

---

experiments were done to prove that the motion of the MagnetoSperm is due to the weak oscillating fields and not due to the gradient of the field [32]. As seen in Figure 2.3, no magnetic fields are applied till  $t = 1.9$  seconds where electromagnets B and D are supplied with uniform currents and A and C are supplied with sinusoidal currents. The MagnetoSperm swims toward electromagnet B until  $t = 4$  seconds where only the sinusoidal currents are turned off and the MagnetoSperm stops swimming. This shows that the motion of the MagnetoSperm is due to the weak oscillating fields and not the gradient of the field. The oscillating fields are then turned on again at  $t = 5.5$  seconds which causes the MagnetoSperm to swim again. The oscillating fields are stopped again at  $t = 7.6$  seconds where the MagnetoSperm also stops swimming. Finally, the oscillating weak magnetic fields are turned on a final time where the MagnetoSperm swims at  $t = 10.8$  seconds. The velocity of the MagnetoSperm in this experiment is  $107 \mu\text{m/s}$  at an oscillating frequency of 50 Hz.

## 2.4 Closed-Loop Control of MagnetoSperm

Closed-loop control is done on the MagnetoSperm as it slides on the bottom of the petri-dish. The oscillating magnetic fields allow the MagnetoSperm to be pulled by the gradient of the field and overcome the strong friction force between the MagnetoSperm and the bottom of the petri-dish. Motion control of the MagnetoSperm is done using the same configuration of electromagnets. However, the electromagnets which produce the oscillating magnetic fields are autonomously switched to change the direction of the MagnetoSperm.

Depending on the reference position, two electromagnets are supplied with square currents to oscillate the head of the MagnetoSperm while the other two electromagnets pull the MagnetoSperm toward the reference.

The position tracking errors between the head of the MagnetoSperm and the reference position are calculated using:

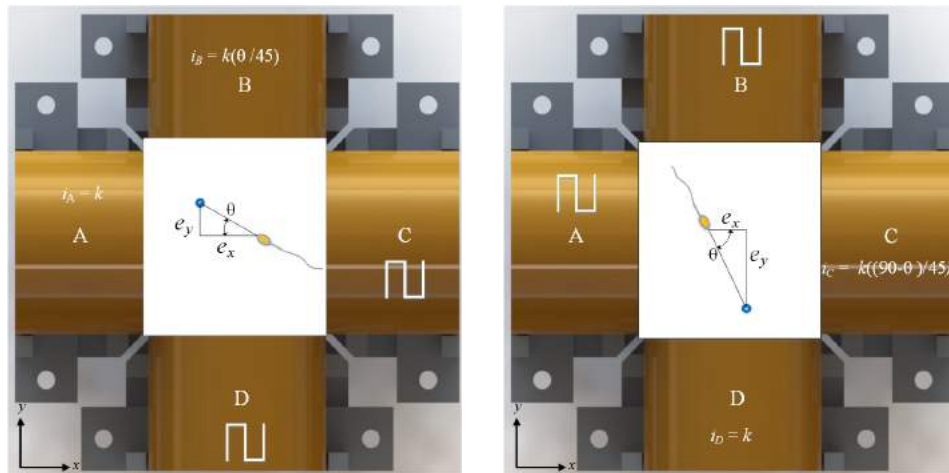
$$e_x = x_{ref} - x \text{ and } e_y = y_{ref} - y, \quad (2.6)$$

where  $e_x$  and  $e_y$  are the position tracking errors along  $x$ - and  $y$ -axis, respectively. Also,  $x_{ref}$  and  $y_{ref}$  are the components of the fixed reference position, and  $x$  and  $y$  are the position of the magnetic head as seen in Figure 2.4. The orientation angle of the MagnetoSperm is given by:

$$\theta = \tan^{-1}\left(\frac{e_x}{e_y}\right). \quad (2.7)$$

The electromagnets which produce the oscillating fields are chosen to be in the opposite direction to the direction of the MagnetoSperm. The other two electromagnets pull the MagnetoSperm towards the reference position using uniform magnetic fields. The direction of the MagentoSperm is controlled by supplying the electromagnets producing the uniform fields with different current magnitudes. The same current magnitude is supplied to both electromagnets, i.e.,  $k$  when  $\theta$  is  $45^\circ$ . In order to orient the MagnetoSperm towards the reference position, the magnitude of the current supplied to one electromagnet must be decreased when  $\theta$  is increased or decreased. The current

supplied to the electromagnet is a ratio between  $\theta$  and  $45^\circ$  multiplied by  $k$ . An example for the MagnetoSperm moving towards the reference position can be seen in Figure 2.4 (a), where  $\theta$  is less than  $45^\circ$ . Electromagnets D and C generate oscillating fields while electromagnets A and B are supplied with uniform currents. Electromagnet A is supplied with a current magnitude of  $k$  while B is supplied with an input of  $k\frac{\theta}{45}$ . In the case when  $\theta$  is more than  $45^\circ$ , the current supply becomes  $k\frac{90-\theta}{45}$  to make the ratio less than 1 as seen in Figure. 2.4 (b).



(a) MagnetoSperm sliding towards reference position (b) MagnetoSperm sliding towards reference position

FIGURE 2.4: Schematic representation of the closed-loop control. Electromagnets A, B, C, and D are used to control the motion of the MagnetoSperm.  $e_x$ ,  $e_y$  and  $\theta$  are the errors in the  $x$  axis and  $y$  axis respectively and the direction of motion. The blue dot indicates the reference position (a) Electromagnets A and B are supplied with uniform currents to control the direction of the MagnetoSperm while electromagnets C and D are supplied with alternating currents to oscillate the head of the MagnetoSperm. (b) Electromagnets C and D are supplied with uniform currents to direct the MagnetoSperm towards the reference position while electromagnets A and B produce alternating magnetic fields.

### 2.4.1 Experimental Results

Characterization of the closed-loop control of MagnetoSperm is done while the MagnetoSperm is sliding on the bottom of the petri-dish. Experiments are done on ellipsoid and triangular magnetic heads to compare velocities between both. Five point-to-point experiments were done for each head at 5 Hz and 45 Hz at different points and the magnetic field applied is about 5 mT. The velocities in the  $x$ -axis,  $y$ -axis and resultant velocities are calculated. Also, as the head of the MagnetoSperm was tracked using the feature tracker, the region of convergence of the head with the reference position in the  $x$ -axis,  $y$ -axis and the resultant region of convergence are calculated. Table 2.1 shows the results for the point to point closed-loop control of the MagnetoSperm with a triangular shaped head and an oscillating frequency of 45 Hz. The head has a length, width and thickness of  $42.6 \mu\text{m}$ ,  $27.7 \mu\text{m}$ , and  $5.2 \mu\text{m}$ , respectively. The rectangular midpiece of the MagnetoSperm has a length,

TABLE 2.1: Point-to-point control of MagnetoSperm with triangular head at a frequency of 45 Hz.  $\mathbf{V}_x$ ,  $\mathbf{V}_y$  and  $\mathbf{V}_r$  are the velocities in the  $x$ -axis,  $y$ -axis and resultant velocity respectively, while  $\mathbf{ROC}_x$ ,  $\mathbf{ROC}_y$  and  $\mathbf{ROC}_r$  are the region of convergence in the  $x$ -axis,  $y$ -axis and resultant region of convergence respectively. Experiments are done at 5 different points. The MagnetoSperm has a length of  $322 \mu\text{m}$  and the magnetic field applied is about 5 mT.

Point	$\mathbf{V}_x(\mu\text{m/s})$	$\mathbf{V}_y(\mu\text{m/s})$	$\mathbf{V}_r(\mu\text{m/s})$	$\mathbf{ROC}_x(\mu\text{m})$	$\mathbf{ROC}_y(\mu\text{m})$	$\mathbf{ROC}_r(\mu\text{m})$
1	6.27	3.04	6.97	4.68	7.03	8.45
2	4.06	14.53	15.09	0	2.34	2.34
3	3.71	0.61	3.76	4.69	4.69	6.63
4	12.11	7.81	14.41	2.35	2.34	3.32
5	7.03	4.69	8.45	2.35	11.72	11.95

width and thickness of  $55 \mu\text{m}$ ,  $8 \mu\text{m}$  and  $5.2 \mu\text{m}$  respectively while the tail is also rectangular with a length, width and thickness of  $225 \mu\text{m}$ ,  $5 \mu\text{m}$ , and  $5.2 \mu\text{m}$ , respectively. The overall length of the MagnetoSperm is  $322.6 \mu\text{m}$ . The velocities and region of convergence in the  $x$ -axis and  $y$ -axis are calculated and then the resultant velocity and region of convergence is derived from them. The least velocities are seen at point number 3 where the velocities in the  $x$  and  $y$  axes are  $3.71 \mu\text{m/s}$  and  $0.61 \mu\text{m/s}$ , respectively. The resultant velocity is calculated to be  $3.76 \mu\text{m/s}$  with a resultant region of convergence of  $6.63 \mu\text{m}$ . The maximum resultant velocity is recorded at point number 2 where the velocity in the  $x$  and  $y$  axes are  $4.06 \mu\text{m/s}$  and  $14.53 \mu\text{m/s}$  respectively and the maximum resultant velocity is  $15.09 \mu\text{m/s}$ . The minimum resultant region of convergence is also observed at point number 2 and is equal to  $2.34 \mu\text{m}$ .

Table 2.2 shows results of the same MagnetoSperm with a triangular shaped head under the influence of an oscillating frequency of  $5 \text{ Hz}$ . Point number 3 gives a much higher resultant velocity compared with the rest of the experiments. The velocities in the  $x$  and  $y$  axes at point number 3 are  $8.79 \mu\text{m/s}$  and  $59.91 \mu\text{m/s}$  respectively and the resultant velocity is  $60.55 \mu\text{m/s}$ . Also, the region of convergence at point number 3 is calculated to be  $10.49 \mu\text{m}$  and is also the minimum region of convergence. The rest of the points show velocities which are relatively close to each other. The minimum resultant velocity is shown at point number 1 with velocities in the  $x$  and  $y$  axes equal to  $4.09 \mu\text{m/s}$  and  $0.83 \mu\text{m/s}$  respectively and a resultant velocity of  $4.17 \mu\text{m/s}$ . Also, the resultant region of convergence for point number 1 is calculated to be  $21.57$

$\mu\text{m}$ . However, the maximum region of convergence is  $42.77 \mu\text{m}$  as seen in point number 5. The fact that point number 3 had a much higher resultant velocity than the rest of the experiments could be attributed to the theory that the MagnetoSperm could have been in a region with a much higher magnetic field gradient which helped in pulling the sliding MagnetoSperm faster. The regions of convergence of the points at a frequency of 5 Hz are relatively higher than the regions of convergence calculated at 45 Hz due to the wider angle the head moves while sliding. It is more difficult for the head to stop near to the reference position at 5 Hz than at 45 Hz.

TABLE 2.2: Point-to-point control of MagnetoSperm with triangular head at a frequency of 5 Hz.  $\mathbf{V}_x$ ,  $\mathbf{V}_y$  and  $\mathbf{V}_r$  are the velocities in the  $x$ -axis,  $y$ -axis and resultant velocity respectively, while  $\mathbf{ROC}_x$ ,  $\mathbf{ROC}_y$  and  $\mathbf{ROC}_r$  are the region of convergence in the  $x$ -axis,  $y$ -axis and resultant region of convergence respectively. Experiments are done at 5 different points. The MagnetoSperm has a length of  $322 \mu\text{m}$  and the magnetic field applied is about 5 mT.

Point	$\mathbf{V}_x(\mu\text{m/s})$	$\mathbf{V}_y(\mu\text{m/s})$	$\mathbf{V}_r(\mu\text{m/s})$	$\mathbf{ROC}_x(\mu\text{m})$	$\mathbf{ROC}_y(\mu\text{m})$	$\mathbf{ROC}_r(\mu\text{m})$
1	4.09	0.83	4.17	16.41	13.99	21.57
2	0.71	4.16	4.22	9.38	18.75	20.97
3	8.79	59.91	60.55	4.69	9.38	10.49
4	5.68	0.21	5.69	7.03	9.37	11.71
5	3.46	2.34	4.18	42.19	7.03	42.77

Table 2.3 shows the results obtained for the MagnetoSperm with an ellipsoid head at an oscillating frequency of 45 Hz. The head has a length, width and thickness of  $42.6 \mu\text{m}$ ,  $27.7 \mu\text{m}$ , and  $5.2 \mu\text{m}$  respectively. The rectangular midpiece of the MagnetoSperm has a length, width and thickness of  $55 \mu\text{m}$ ,  $8 \mu\text{m}$  and  $5.2 \mu\text{m}$  respectively while the tail is also rectangular with a length,

width and thickness of  $225 \mu\text{m}$ ,  $5 \mu\text{m}$ , and  $5.2 \mu\text{m}$ . The overall length of the MagnetoSperm is  $322.6 \mu\text{m}$ . The minimum resultant velocity is  $4.83 \mu\text{m/s}$  at point number 5 with  $x$  and  $y$  components equal to  $1.17 \mu\text{m/s}$  and  $4.69 \mu\text{m/s}$  respectively. The resultant region of convergence in this experiment is  $18.9 \mu\text{m}$ . The maximum resultant velocity is found at point number 2 to be  $7.93 \mu\text{m/s}$  with  $x$  and  $y$  components  $7.39 \mu\text{m/s}$  and  $2.88 \mu\text{m/s}$  respectively.

TABLE 2.3: Point-to-point control of MagnetoSperm with elliptical head at a frequency of 45 Hz.  $\mathbf{V}_x$ ,  $\mathbf{V}_y$  and  $\mathbf{V}_r$  are the velocities in the  $x$ -axis,  $y$ -axis and resultant velocity respectively, while  $\mathbf{ROC}_x$ ,  $\mathbf{ROC}_y$  and  $\mathbf{ROC}_r$  are the region of convergence in the  $x$ -axis,  $y$ -axis and resultant region of convergence respectively. Experiments are done at 5 different points. The MagnetoSperm has a length of  $322 \mu\text{m}$  and the magnetic field applied is about 5 mT.

Point	$\mathbf{V}_x(\mu\text{m/s})$	$\mathbf{V}_y(\mu\text{m/s})$	$\mathbf{V}_r(\mu\text{m/s})$	$\mathbf{ROC}_x(\mu\text{m})$	$\mathbf{ROC}_y(\mu\text{m})$	$\mathbf{ROC}_r(\mu\text{m})$
1	7.21	0.18	7.21	9.37	16.41	18.90
2	7.39	2.88	7.93	18.75	4.69	19.33
3	0.43	5.75	5.77	11.72	18.75	22.11
4	4.76	0.85	4.84	7.03	18.75	20.02
5	1.17	4.69	4.83	18.75	2.34	18.90

The results for the point-to-point control of the MagnetoSperm with an elliptical head at 5 Hz are shown in table 2.4. The minimum resultant velocity is calculated to be  $10.09 \mu\text{m/s}$  with  $x$  and  $y$  components of  $6.22 \mu\text{m/s}$  and  $7.95 \mu\text{m/s}$ . This is larger than all experiments done with the MagnetoSperm with the elliptical head at 45 Hz. Also, the resultant region of convergence in the experiment is  $46.05 \mu\text{m}$ . Point number 5 gives the maximum resultant velocity where the components in the  $x$  and  $y$  axes are  $35.16 \mu\text{m/s}$  and  $7.42 \mu\text{m/s}$  respectively and the resultant velocity is  $35.93 \mu\text{m/s}$ .

TABLE 2.4: Point-to-point control of MagnetoSperm with elliptical head at a frequency of 5 Hz.  $\mathbf{V}_x$ ,  $\mathbf{V}_y$  and  $\mathbf{V}_r$  are the velocities in the  $x$ -axis,  $y$ -axis and resultant velocity respectively, while  $\mathbf{ROC}_x$ ,  $\mathbf{ROC}_y$  and  $\mathbf{ROC}_r$  are the region of convergence in the  $x$ -axis,  $y$ -axis and resultant region of convergence respectively. Experiments are done at 5 different points. The MagnetoSperm has a length of  $322 \mu\text{m}$  and the magnetic field applied is about 5 mT.

Point	$\mathbf{V}_x(\mu\text{m/s})$	$\mathbf{V}_y(\mu\text{m/s})$	$\mathbf{V}_r(\mu\text{m/s})$	$\mathbf{ROC}_x(\mu\text{m})$	$\mathbf{ROC}_y(\mu\text{m})$	$\mathbf{ROC}_r(\mu\text{m})$
1	6.22	7.95	10.09	11.72	44.53	46.05
2	23.26	2.34	23.38	0	30.47	30.47
3	1.26	13.52	13.58	23.44	21.09	31.53
4	20.05	9.90	22.36	14.06	9.37	16.90
5	35.16	7.42	35.93	32.81	23.44	40.32

The main conclusion which could be deduced from these results is the relationship between the oscillating magnetic frequency and the region of convergence. As the head is targeted by the feature tracking software, the position error at low frequencies is larger than at high frequencies also due to the larger angle of rotation of the head. As the rotation of the head at 5 Hz is larger than at 45 Hz this increases the difficulty of the head reaching the reference position. As the alternating magnetic fields produce a force that overcomes the drag force, the gradient then has an influence on the motion of the MagnetoSperm. The gradient alone cannot pull the MagnetoSperm without producing alternating magnetic fields. This gives rise to the problem that the motion of the MagnetoSperm is mainly dependant on the direction of the gradient. This can be shown when the MagnetoSperm swims backwards for example. That is why the closed-loop control of the MagnetoSperm could only be done in the center of the work space where the gradients almost cancel each other. Outside a

certain region, the control law does not hold and the MagnetoSperm will swim in totally different directions dependant on the resultant gradient acting on it from the four electromagnets. This can also be seen in the wide deviation between the velocities as the gradient acting on the MagentoSperm changes from one point to another. There are two proposals to overcome this problem. First, a full map of the gradients should be incorporated in the control law to allow it to be reliable outside the center of the work space. Second, at high magnification, the motion of the tail of the MagnetoSperm is shown to not have a sinusoidal motion as that of human sperm. The motion of the tail is rigid and it alternates as if it is cutting the water. This may be the reason why the propulsive force of the MagnetoSperm is not the main dominant force which drives the MagentoSperm forward. For future manufacturing, the tail of the MagentoSperm should be flexible enough to bend in a sinusoidal motion

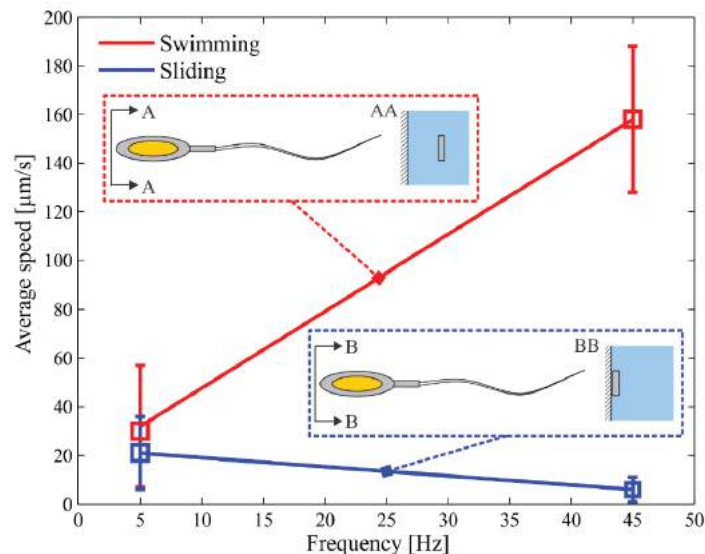
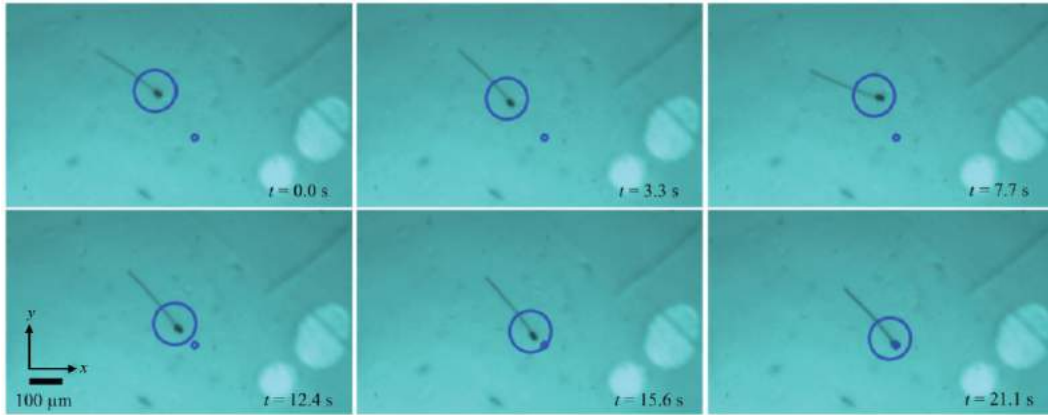
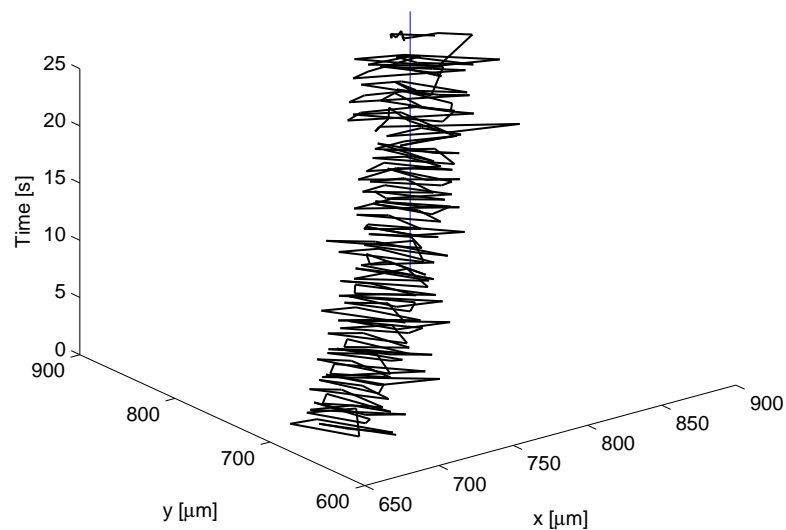


FIGURE 2.5: Swimming and sliding speeds of MagnetoSperm at 5 Hz and 45 Hz. The swimming speeds are calculated using open-loop control trails while sliding speeds are calculated using closed-loop control trails. The MagnetoSperm swims while fully immersed in water and slides while in contact with the bottom.

in order to provide a larger propulsive force. The question which arises next would be "Which is the best frequency to produce the highest sliding velocity?". As only 2 frequencies are used in these experiments and the velocities are calculated at different points it is not possible to make such a deduction. However, the next chapter raises this question and provides experiments to reach such a conclusion.

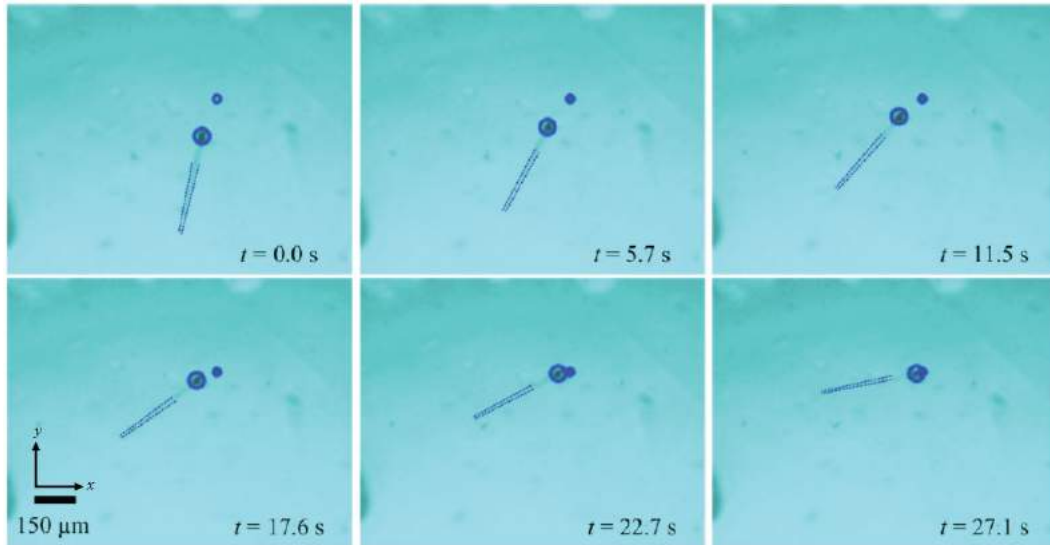


(a) Closed-loop motion control of a MagnetoSperm with an ellipsoid head. The MagnetoSperm slides on the bottom of the petri-dish to reach the reference position at a velocity of  $12 \mu\text{m/s}$ . The oscillating magnetic fields are produced at 5 Hz. The blue circle is assigned using a feature tracking algorithm and indicates the head of the MagnetoSperm. The small blue circle indicates the reference position.

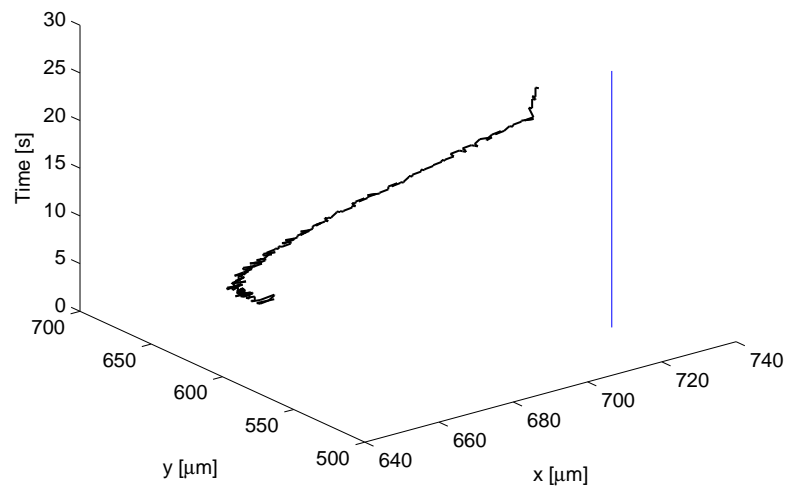


(b) Graphical plot of the position of the magnetic head against time. The blue line indicates the reference position.

FIGURE 2.6: Point-to-Point closed-loop control of the MagnetoSperm at 5 Hz. (a) The MagnetoSperm slides on the bottom of the petri-dish to reach its reference position. A feature tracking algorithm is used to track the MagnetoSperm and control its motion. (b) Graphical plot of the point-to-point motion control of the MagnetoSperm.



(a) Closed-loop motion control of a MagnetoSperm with an ellipsoid head. The MagnetoSperm slides on the bottom of the petri-dish to reach the reference position at a velocity of  $5 \mu\text{m/s}$ . The oscillating magnetic fields are produced at 45 Hz. The blue circle is assigned using a feature tracking algorithm and indicates the head of the MagnetoSperm. The small blue circle indicates the reference position. The dashed blue lines indicate the flexible tail.



(b) Graphical plot of the position of the magnetic head against time. The blue line indicates the reference position.

FIGURE 2.7: Point-to-Point closed-loop control of the MagnetoSperm at 45 Hz. (a) The MagnetoSperm slides on the bottom of the petri-dish to reach its reference position. A feature tracking algorithm is used to track the MagnetoSperm and control its motion. (b) Graphical plot of the point-to-point motion control of the MagnetoSperm.

# Chapter 3

## Sliding Microparticles

In the previous chapter, the MagnetoSperm is controlled while sliding on the surface of a petri-dish. This chapter shows the use of sliding microparticles to characterize the sliding motion against a range of different frequencies. As magnetic microparticles have the potential to be used as targeted drug carriers (please refer to Appendix B), there is a possibility that they do not only swim to their reference positions but also slide on the lumen of the blood veins in order to reach the targeted diseased cells as seen in Figure 3.1. However, due to the large friction forces between the microparticles and the lumen of the blood veins, large magnetic fields would be needed to pull magnetic drug carriers. In this chapter, experiments on the effect of oscillating magnetic fields to increase the velocity of sliding microparticles are done. The motion of clusters of microparticles is characterized against the frequency of the oscillating field and the number of microparticles used in a cluster. Also, closed-loop point-to-point control is applied and the sliding particles are driven in a circular

trajectory.

### 3.1 Modelling of the Sliding Microparticles

The equation which governs the motion of a cluster of microparticles while sliding on a surface such as the lumen of a blood vein or the bottom of a petri-dish constitutes of the magnetic force which pulls the sliding microparticles, the fluid drag force and the surface friction force, this is given by:

$$\nabla (\mathbf{m}(\mathbf{P}) \cdot \mathbf{B}(\mathbf{P})) + F_c \eta \dot{\mathbf{P}} + \mu_s m_c \mathbf{g} = 0, \quad (3.1)$$

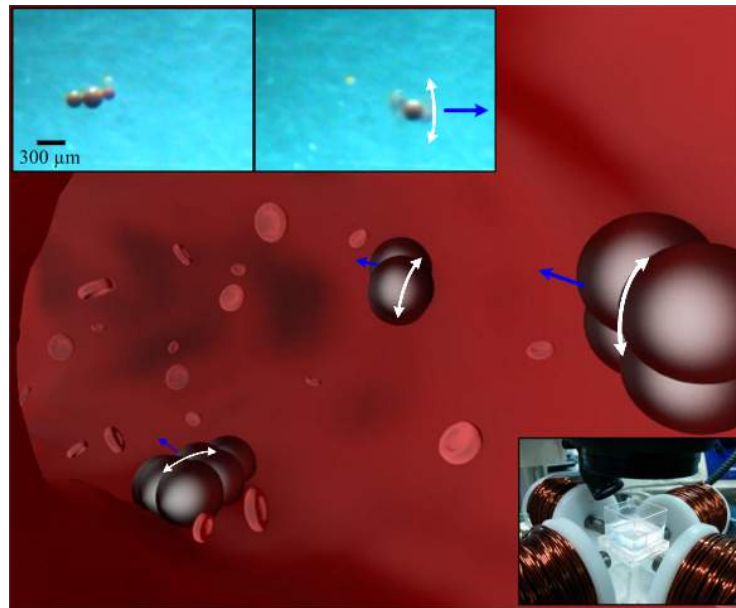
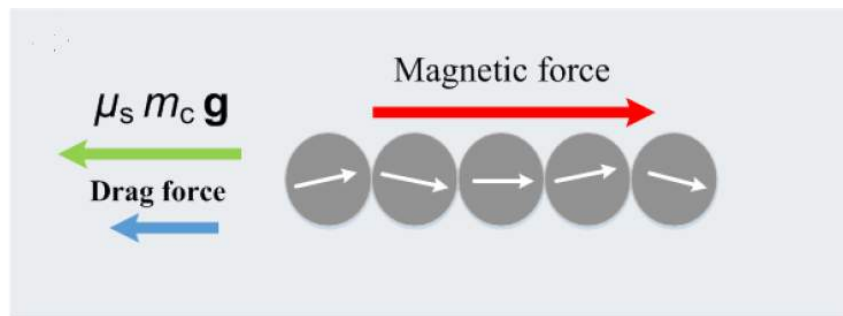
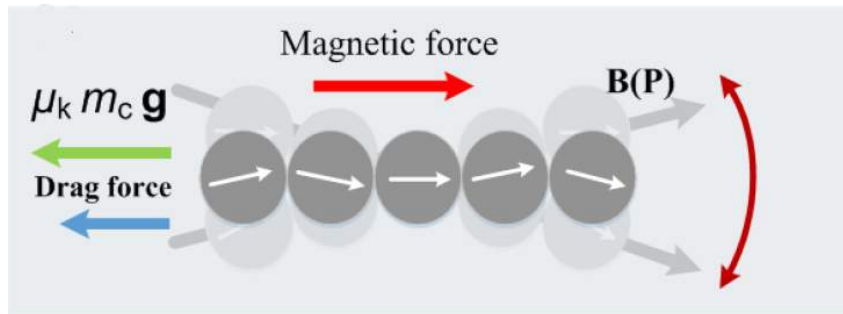


FIGURE 3.1: Schematic representation of microparticles sliding on the lumen of blood veins. The white arrows represent the magnetic field oscillations which allow the microparticles to overcome the static friction. The microparticles are pulled by the weak magnetic field gradients represented by blue arrows. Experiments are done using clusters of microparticles (as seen in the inset on the top-left corner) using the electromagnetic setup shown in the bottom-right corner. This schematic representation is designed using Blender (Blender 2.71, Blender Foundation, Entrepotdok, Amsterdam, The Netherlands).

where  $F_c$  and  $m_c$  are the shape factor of the cluster and the mass of the cluster, respectively. In order for the microparticles to slide on the surface, the gradient of the magnetic field must overcome the static surface friction between the microparticles and the surface. Relatively large magnetic field gradients are therefore needed to pull the particles. However, by applying oscillating magnetic fields, the microparticles align along the oscillating magnetic field lines and overcome the static surface friction. The kinetic surface friction acts



(a) Schematic showing sliding microparticles without oscillating magnetic fields.



(b) Schematic showing sliding microparticles with oscillating magnetic fields.

FIGURE 3.2: Schematic representation showing the modelling of the sliding microparticles. The green arrow indicates the friction force. The blue arrow indicates the drag force while the red arrow indicates the magnetic force. The magnetic force is larger when oscillating magnetic fields are not applied. (a) The forces exerted on the sliding microparticles without oscillating fields. (b) The forces exerted on the sliding microparticles with oscillating microparticles.

on the particles instead, therefore the equation of motion is changed to:

$$\nabla (\mathbf{m}(\mathbf{P}) \cdot \mathbf{B}(\mathbf{P})) + F_c \eta \dot{\mathbf{P}} + \mu_k m_c \mathbf{g} = 0, \quad (3.2)$$

where  $\mu_k$  is the coefficient of kinetic surface friction. As  $\mu_k < \mu_s$ , this means that the gradient of the magnetic field needed to pull the particles is less compared to the motion without oscillation. Figure 3.2 shows a schematic representation of the forces acting on the sliding microparticles. The next section will explain the electromagnetic setup used to control the sliding microparticles.



FIGURE 3.3: Electromagnetic setup used for the characterization and control of the microparticles. The setup consists of an orthogonal array of electromagnets to produce the oscillating magnetic fields in order to overcome the static friction and the magnetic field gradient to pull the particles. An optical microscope is used to track the motion of the particles. The bottom-left inset shows a cluster of 9 particles oscillating due to the alternating magnetic fields represented by the white arrows. The red arrow represents the direction of motion of the particles.

---

## 3.2 Electromagnetic System

The electromagnetic system used in these experiments consists of four electromagnetic coils in an orthogonal array. These electromagnetic coils produce the alternating magnetic fields to overcome the static surface friction and pull the sliding microparticles. Each coil has an inner-diameter, outer diameter, length and number of turns 10 mm, 50 mm, 60 mm and 1200 turns, respectively. The coils provide a maximum magnetic field of 14.5 mT and magnetic field gradient of 0.9 T/m at the center of the workspace (10 mm $\times$ 10 mm). The coils are supplied by electric currents using electric drivers (MD10C, Cytron Technologies Sdn. Bhd, Kuala Lumpur, Malaysia) and controlled using an Arduino control board (Arduino UNO - R3, Arduino, Memphis, Tennessee, U.S.A) and Simulink (MathWorks, Natick, Massachusetts, U.S.A). An optical microscope is used (Stemi 2000-C, Carl Zeiss Microscopy, LLC, New York, U.S.A) to track the motion of the microparticles. The setup can be seen in Figure 3.3.

## 3.3 Experimental Results

A proof of concept experiment is first done to show the effect of applying alternating magnetic fields when pulling a cluster of microparticles. Then, the frequency response of the microparticles is measured by calculating the velocity of clusters of microparticles at a frequency range from 5 Hz to 55

Hz. Finally, closed-loop control is done to drive the microparticles to different points and also through a circular trajectory.

### **3.3.1 Proof of Concept**

This experiment shows that applying a constant field is not enough to pull the microparticles while they are in contact with the surface. A cluster of 3 microparticles is used as seen in Figure 3.4. A constant magnetic field is applied throughout the experiment. The microparticles do not move until the alternating magnetic fields are applied at  $t = 2$  seconds. The microparticles then move until the alternating fields are stopped at  $t = 2.4$  seconds where the constant field is not able to overcome the friction force. The procedure is then repeated at  $t = 4.5$  seconds where the microparticles are able to break free of the static friction and slide at a speed of  $300 \mu\text{m/s}$ .

### **3.3.2 Frequency Response of Clusters of Microparticles**

Characterization of the sliding microparticles is done at a constant magnetic field gradient of  $0.9 \text{ m/T}$  over a frequency range from  $5 \text{ Hz}$  to  $50 \text{ Hz}$ . The speed of the clusters are measured to observe its relationship with applying different frequencies. Clusters of 3 to 4 particles and 5 to 9 particles were used in the experiments. Clusters more than 9 particles tend to break into smaller clusters therefore their results are not taken into consideration. As can be seen in Figure 3.5, the average speed of the microparticles increase with the increase of the oscillating frequency. At  $5 \text{ Hz}$ , the cluster of 3 to 4

particles slide at an average speed of  $415.6 \mu\text{m/s}$  while the cluster of 6 to 9 microparticles slides at an average speed of  $722.5 \mu\text{m/s}$ . This gives a difference in speed of  $306.9 \mu\text{m/s}$ . This difference decreases gradually as the oscillating frequency increases till 20 Hz. At 20 Hz, the cluster of 3 to 4 particles slides with an average speed of  $777.2 \mu\text{m/s}$  and the cluster of 6 to 9 microparticles slides at an average speed of  $1002.8 \mu\text{m/s}$  giving a difference in speed of  $225.6 \mu\text{m/s}$ . However at 25 Hz, there is a high increase in average sliding speed of the cluster with 6 to 9 microparticles. The sliding speed at 25 Hz of the cluster with 6 to 9 particles is  $1343.9 \mu\text{m/s}$  while the average sliding speed of the cluster with 3 to 4 microparticles is  $822.7 \mu\text{m/s}$  giving a difference in speed of  $491.2 \mu\text{m/s}$ . The highest sliding speed for both clusters appears at 30 Hz where the average sliding speed of the cluster with 3 to 4 particles is

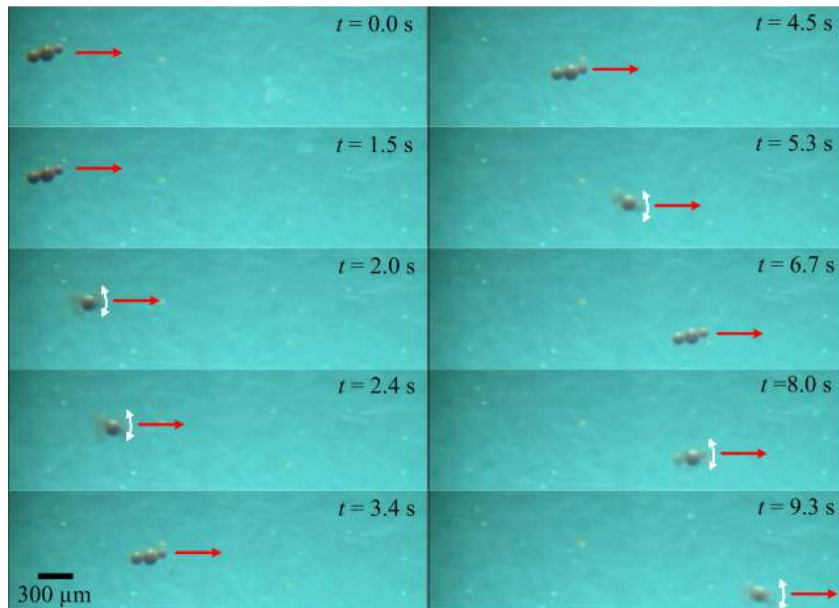


FIGURE 3.4: A constant magnetic field are applied to a cluster of 3 microparticles throughout the experiment. Alternating magnetic fields are turned on and off over the length of the experiment. The red arrow represents the constant field while the the white arrow represents the alternating fields. The alternating fields are applied after  $t = 1.5$  seconds,  $t = 4.5$  seconds and  $t = 6.7$  seconds. The microparticles overcome the static friction and slide at a velocity of  $300 \mu\text{m/s}$  at a frequency of 30 Hz.

1056.7  $\mu\text{m/s}$  and the average sliding speed of the cluster with 6 to 9 particles is 1798.9  $\mu\text{m/s}$ . At 35 Hz, the average sliding speed of the cluster with 6 to 9 particles only decreases to 1499.9  $\mu\text{m/s}$  while the average sliding speed of the cluster with 3 to 4 particles becomes 780  $\mu\text{m/s}$ . A steady decrease in velocity of both clusters is observed till 50 Hz where the average sliding speed of the 3 to 4 particles is 557.7  $\mu\text{m/s}$  and the average sliding speed of the cluster with 6 to 9 particles is 848  $\mu\text{m/s}$ . However, the average sliding speed of 6 to 9 particles increase slightly at 55 Hz to 959.1  $\mu\text{m/s}$ . Overall, the maximum average speed for both groups of clusters is found at 30 Hz where the speed decreases to about 50% at a frequency of 50 Hz. As the magnetic dipole moment of the cluster with 5 to 9 particles is greater than the one with 3 to

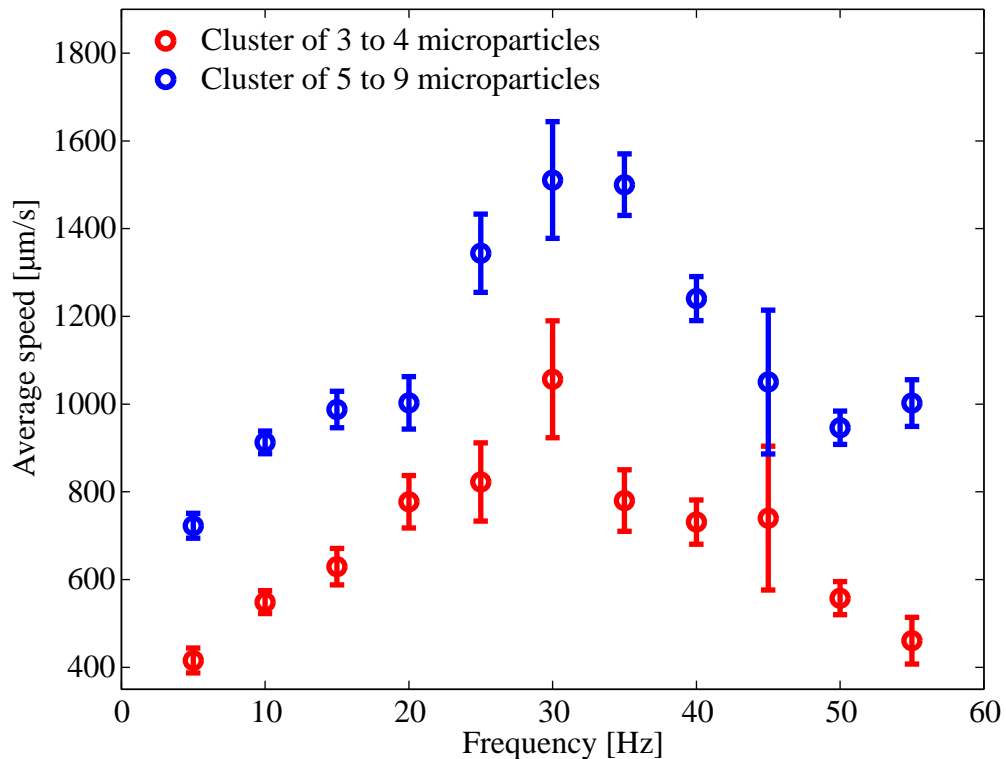


FIGURE 3.5: Frequency response of clusters of sliding microparticles. Clusters of 3 to 4 and 5 to 9 microparticles are used in the experiments. The average velocity of 5 trials is calculated at each frequency. The clusters have zero speed when no oscillation are applied. A constant gradient of 0.9 T/m is applied through all the experiments.

---

4 particles, they have an approximate 30% increase in speed compared to the cluster of 3 to 4 particles. Figure 3.7 shows one experiment where a cluster of 3 microparticles are moved along the  $x$ -axis. This representative experiment is done at a frequency of 40 Hz and shows a velocity of  $890 \mu\text{m/s}$ .

The effect of the oscillating magnetic fields is also investigated on the magnitude of the constant field gradient required to pull the microparticles as seen in Figure 3.6. First, the gradient of the magnetic field is gradually increased while not applying any alternating magnetic fields. The microparticles start to move at a constant magnetic field of 13.4 mT. Next, the experiment is repeated 10 times with a frequency range of 5 Hz to 50 Hz. The microparticles start to move at an average magnetic field of 3.37 mT. This shows a 75% decrease in the magnetic field needed to pull the cluster when oscillating magnetic fields are applied.

### **3.3.3 Closed-Loop Control of the Cluster of Sliding Microparticles**

Closed-loop control is done on the sliding micro-particles using the same orthogonal configuration of electromagnets. When the reference position is set, the error is calculated and the electromagnets are autonomously switched to control the direction of the sliding microparticles. Two electromagnets produce oscillating magnetic fields while the other two are provided with constant currents to pull the microparticles.

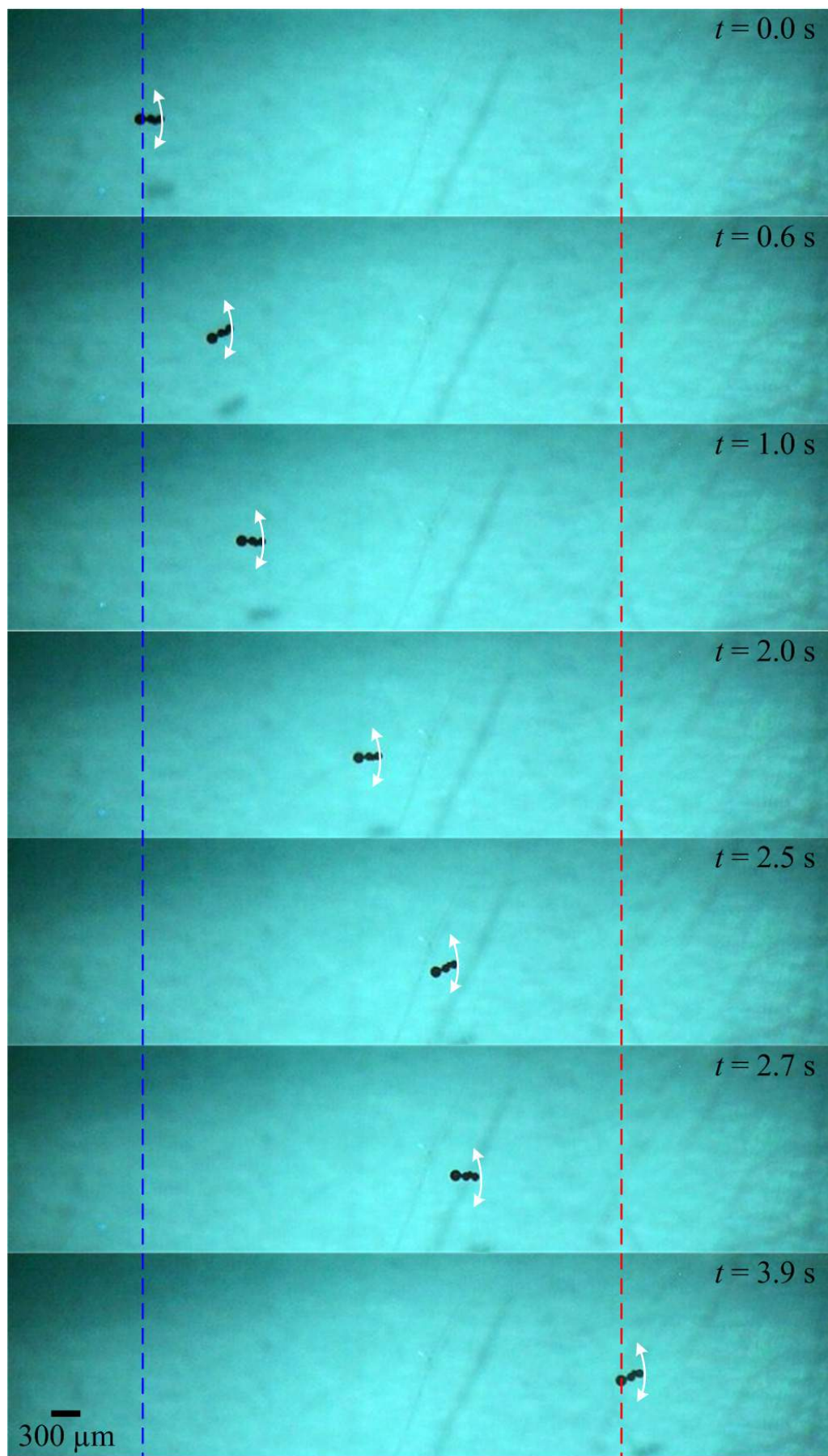


FIGURE 3.7: Microparticles sliding on the surface of a petri-dish at a oscillating frequency of 40 Hz and an average speed of 3 body lengths per second. The white arrows indicate the oscillating magnetic fields while the blue and red dashed lines indicate the start and ending positions of the microparticles.

The position tracking errors between the sliding microparticles and the reference position are calculated by:

$$e_x = x_{ref} - x \text{ and } e_y = y_{ref} - y, \quad (3.3)$$

where  $e_x$  and  $e_y$  are the position tracking errors along the  $x$ - and  $y$ - axis, respectively. Also,  $x$  and  $y$  are the position of the cluster along the  $x$ - and  $y$ - axis, respectively. Further,  $x_{ref}$  and  $y_{ref}$  are the components of the fixed reference position. The position of the cluster relative to the reference position determines the electromagnets which produce the uniform field. The constant currents provided to the the electromagnets producing the uniform field is given by:

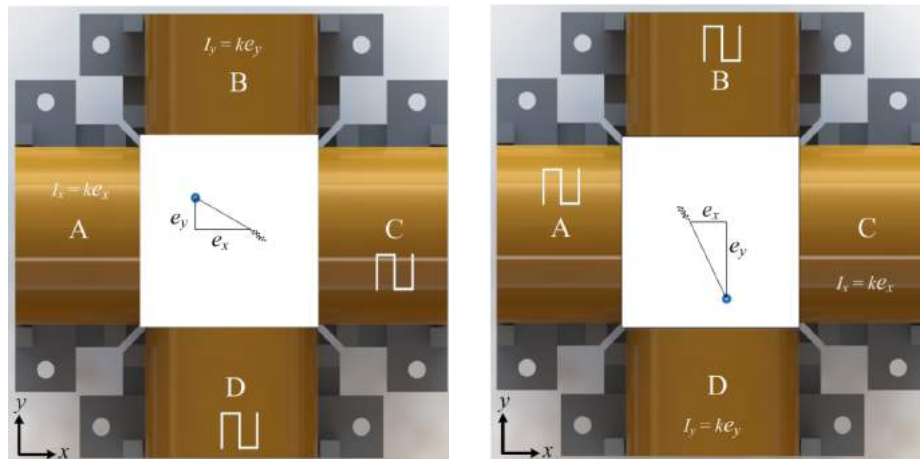
$$I_x = ke_x \text{ and } I_y = ke_y, \quad (3.4)$$

where  $I_x$  and  $I_y$  are the current magnitudes of each electromagnet and  $k$  is the proportional gain. The representative motion control results are shown in Figure 3.9. The oscillating magnetic field orients towards the reference position once it is given to the closed-loop control system. The clusters then break free of the static friction and slide toward 4 different reference positions. The first reference position is give at  $t = 2.6$  seconds where the microparticles slide to the right and reach the reference position at  $t = 18$  seconds with a speed of  $116.9 \mu\text{m/s}$ . Second reference position is given  $t = 20$  seconds where the microparticles slide with a speed of  $471.7 \mu\text{m/s}$  and reach the reference position at  $t = 20$  seconds. At  $t = 34.2$  seconds the third reference position is set and the microparticles slide at a speed of  $350 \mu\text{m/s}$ . The microparticles

finally slide at a speed of  $70 \mu\text{m/s}$  to reach the final reference position at  $t = 70$  seconds. The average sliding speed measured is  $223 \mu\text{m/s}$  and the maximum position tracking error is  $20 \mu\text{m}$ . The variations in the speeds is due to the fact of the difference of the gradient at different reference positions.

Using the same control method, the microparticles are driven through a circular trajectory as seen in Figure 3.10. Twenty reference points are assigned to form a circle of diameter  $1904 \mu\text{m}$  which the microparticles slide on. An average velocity of  $60 \mu\text{m/s}$  is calculated.

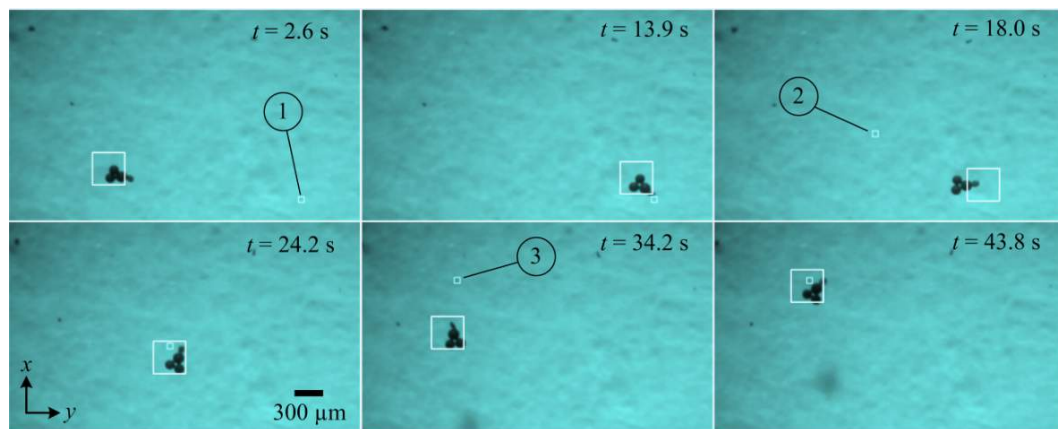
This chapter shows the influence of oscillating fields on sliding microparticles. Some questions arise from the observations seen in this chapter. Producing



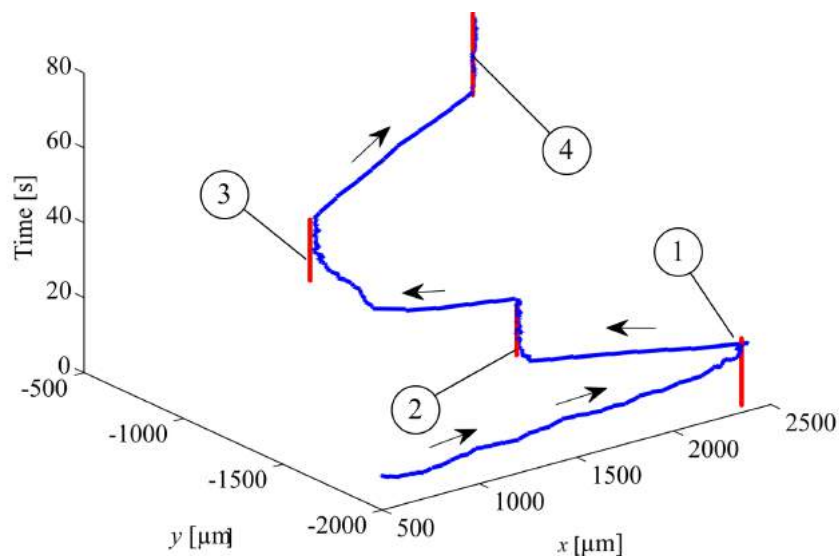
(a) Microparticles sliding towards reference position      (b) Microparticles sliding towards reference position

FIGURE 3.8: Schematic representation of the closed-loop control. Electromagnets A, B, C, and D are used to control the motion of the Microparticles.  $e_x$ ,  $e_y$  and  $\theta$  are the errors in the  $x$  axis and  $y$  axis respectively and the direction of motion. The blue dot indicates the reference position (a) Electromagnets A and B are supplied with uniform currents to control the direction of the Microparticles while electromagnets C and D are supplied with alternating currents to oscillate the head of the Microparticles. (b) Electromagnets C and D are supplied with uniform currents to direct the Microparticles towards the reference position while electromagnets A and B produce alternating magnetic fields.

oscillating fields could help facilitate the motion of other microrobots not experimented on in this thesis. Also, whether these oscillations could be enough to resist the high static friction forces found on the lumen of blood vessels is still a mystery. The orientation of the microparticles when a constant gradient



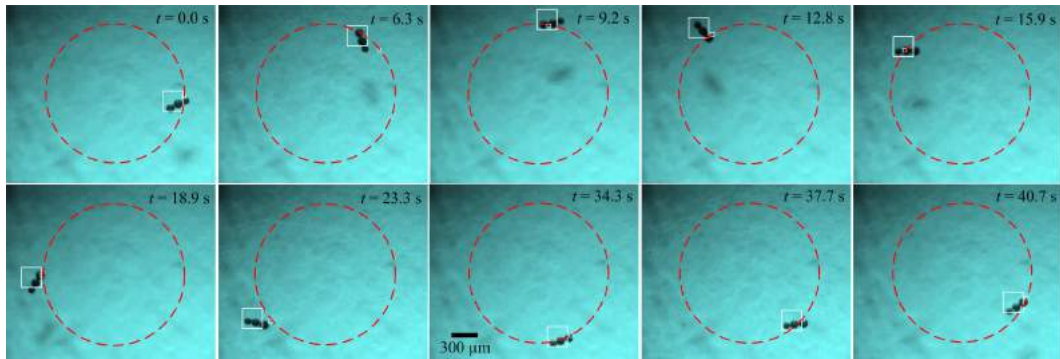
(a) Point-to-point closed-loop control of sliding microparticles. The microparticles slide on the bottom of the petri-dish to reach the reference positions.



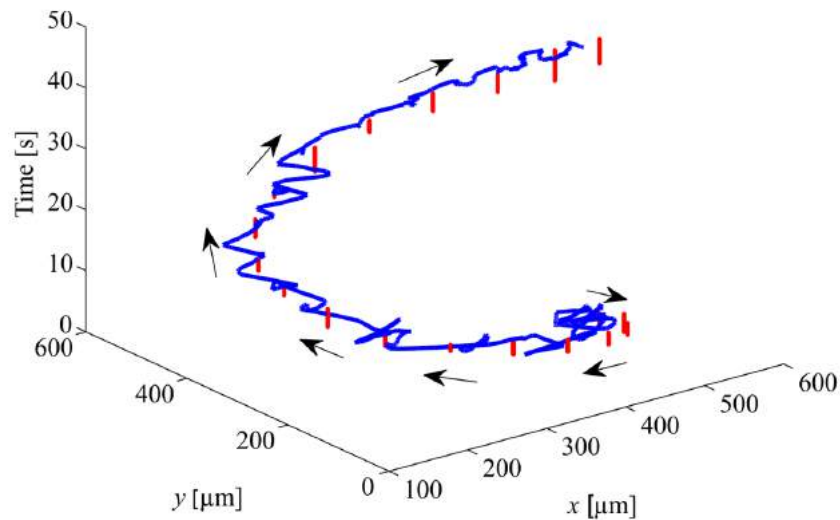
(b) Graphical plot of the position of the microparticles against time. The red lines indicate the reference positions.

FIGURE 3.9: Closed-loop control of sliding microparticles. a) The microparticles slide toward 3 different reference positions. The average speed calculated is  $223 \mu\text{m/s}$  and the maximum steady-state error is  $20 \mu\text{m}$ . b) The red vertical lines represent the reference positions (which are represented by the small white squares in the snap-shots). The blue lines indicate the trajectory of the microparticles.

is applied should be taken into consideration. The particles tend to form a straight line everytime a constant gradient is applied. When oscillating frequencies are applied, the particles oscillate and slide on the surface in a snake like motion. This arises the possibility of having self-assembled sperm-shaped



(a) Circular trajectory of sliding microparticles. The microparticles slide on the bottom of the petri-dish to reach the reference positions and slide in a circular trajectory.



(b) Graphical plot of the position of the microparticles against time. The red lines indicate the reference positions.

FIGURE 3.10: Closed-loop control of sliding microparticles in a circular trajectory. a) 20 reference positions identify circular trajectory with a diameter of  $1904 \mu\text{m}$ . The average velocity of the microparticles is  $60 \mu/\text{s}$ . b) The blue line indicates the path of the microparticles and the dashed-red circle indicates the reference circular trajectory. The direction of the cluster and the position of the cluster are indicated by the black arrows and the white squares respectively.

robots where the microparticles would be originally separated and then assemble together when a constant field is applied. The sperm-shaped robot would then propagate when the oscillating magnetic fields are applied.

# Chapter 4

## Conclusions

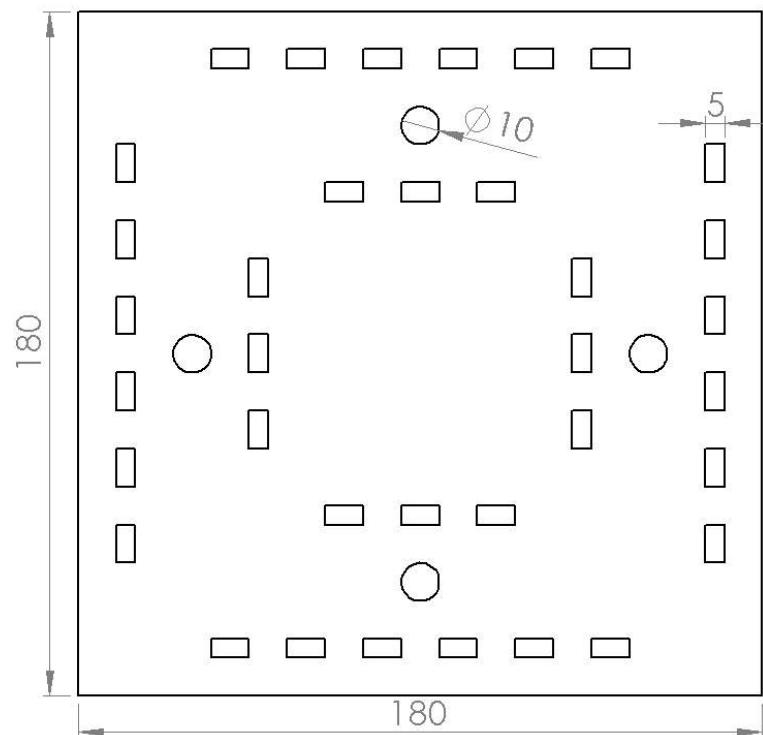
This work presents research in two main areas. First the closed-loop control of a sperm-shaped microrobot which we refer to as MagentoSperm is done. Point-to-point control is done using an electromagnetic setup with closed-configuration consisting of four electromagnets. The MagentoSperms slide toward their reference positions. MagentoSperms with ellipsoid and triangular heads are used in these experiments. Five reference points are given for each MagentoSperm at frequencies of 5 Hz and 45 Hz. The MagentoSperm with the triangular head has a maximum velocity of  $15.09 \mu\text{m/s}$  at 45 Hz and a maximum velocity of  $60.55 \mu\text{m/s}$  at 5 Hz. The MagentoSperm with the elliptical head has a maximum velocity of  $7.93 \mu\text{m/s}$  at 5 Hz and a maximum velocity of  $35.93 \mu\text{m/s}$  at 45 Hz. The main conclusion deduced is that the position tracking error increases as the frequency decreases due to the large rotational angle of the head of the MagentoSperm at low frequencies.

Second, the characterization and control of sliding microparticles is also investigated in this thesis. A range of frequencies are applied from 5 Hz to 55 Hz on clusters of 3 to 4 microparticles and 5 to 9 microparticles. Both clusters experience a maximum velocity at oscillating magnetic fields of 30 Hz. Clusters from 3 to 4 microparticles have an approximate velocity of  $1050 \mu\text{m/s}$  at 30 Hz while clusters of 5 to 9 microparticles have an approximate velocity of  $1500 \mu\text{m/s}$ . Also, the needed magnetic field to pull the microparticles is  $13,4 \text{ mT}$  when no oscillating fields are applied compared with  $3.37 \text{ mT}$  when oscillating fields are applied. This shows a 75 % decrease in magnetic field needed when alternating magnetic fields are applied. Closed-loop point-to-point control is done on the sliding microparticles where an average velocity of  $223 \mu\text{m/s}$  and a steady-state error of  $20 \mu\text{m}$  is measured. The microparticles are also controlled in a circular trajectory with a diameter of  $1904 \mu\text{m}$ . The average velocity measured in this experiment is  $60 \mu\text{m/s}$ .

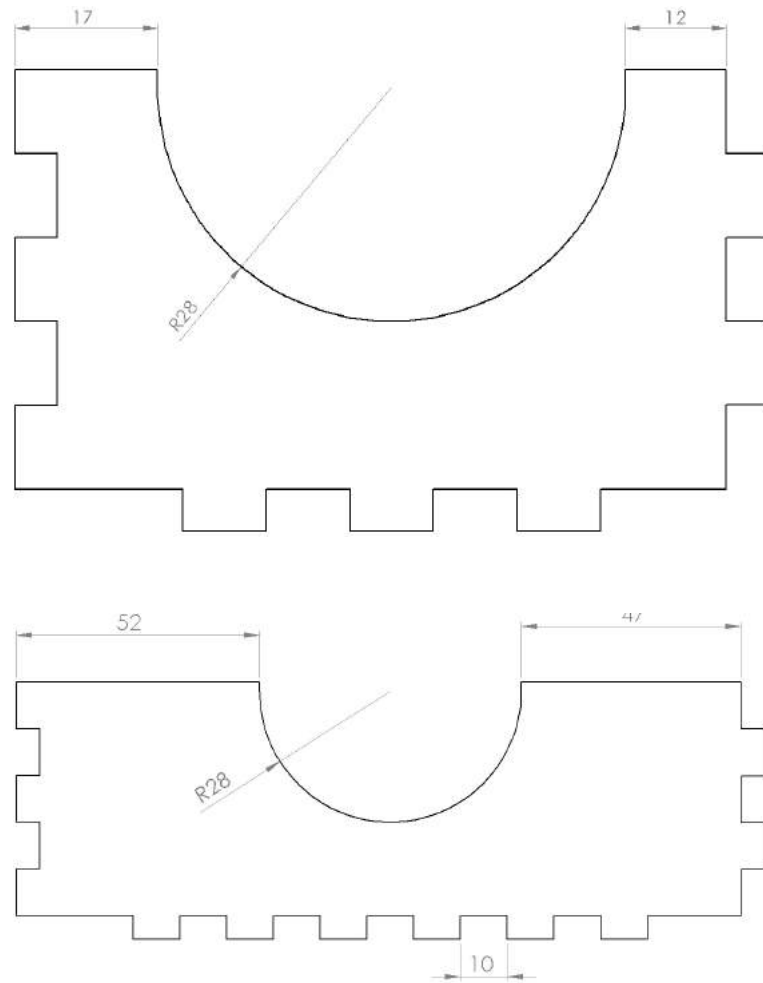
# Appendix A

## Setup Design

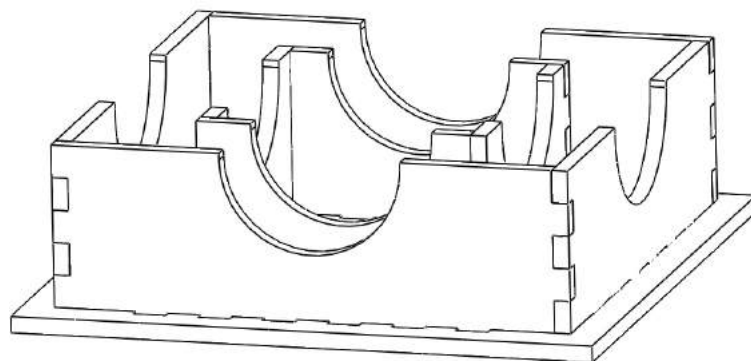
### A.1 Base



## A.2 Holders



## A.3 Assembly



# Appendix B

## Microparticles Data Sheet

# TECHNICAL DATA SHEET



## micromod Partikeltechnologie GmbH

Friedrich-Barnewitz-Str. 4  
D-18119 Rostock  
Germany

Telephone: + 49 381 / 54 34 56 10  
Fax: + 49 381 / 54 34 56 20  
E-mail address: [info@micromod.de](mailto:info@micromod.de)

<b>Product code:</b>	12-00-105
<b>Product name:</b>	PLA-M
<b>Surface:</b>	plain
<b>Size:</b>	100 µm
<b>Solid content:</b>	10 mg/ml
<b>Composition:</b>	magnetic poly(lactic acid) particles
<b>Standard deviation:</b>	)*
<b>Shape:</b>	spherical
<b>Density:</b>	1.3 g/ccm
<b>Magnetization:</b>	4.3 emu/g particles (H =1000 Oe)
<b>Saturation magnetization:</b>	> 6.6 emu/g particles (H > 10.000 Oe)
<b>Stable in:</b>	aqueous buffers pH > 4
<b>Not stable in:</b>	organic solvents, acidic solutions pH < 4
<b>Product form:</b>	suspension in water
<b>Particles per ml:</b>	1.5*10E4
<b>Particles per mg:</b>	1.5*10E3
<b>Colour:</b>	dark brown
<b>Additional remarks:</b>	Storage at 2 - 8°C for 6 months
<b>TECHNOTES:</b>	)* Size cut: 70 µm - 150 µm

# Bibliography

- [1] M. P. Kummer, J. J. Abbott, B. E. Kartochovil, R. Borer, A. Sengul, and B. J. Nelson, OctoMag: an electromagnetic system for 5-DOF wireless micromanipulation, *IEEE Transactions on Robotics*, vol. 26, no. 6, pp. 1006-1017, December 2010.
- [2] S. Martel and M Mohammadi, "Using a swarm of self-propelled natural microrobots in the form of flagellated bacteria to perform complex micro-assembly tasks", *IEEE International Conference of Robotics and Automation (ICRA)*, May 2010.
- [3] S. Sanchez, A. A. Solovev, Sabine Schulze and Oliver G. Schmidt, "Controlled manipulation of multiple cells using catalytic microbots", *Chemical Communications*, vol. 47, pp. 698-700, January 2011.
- [4] W. Wang, L. A. Castro, M. Hoyos, T. E. Mallouk, "Autonomous motion of metallic microrods propelled by ultrasound", *ACS Nano*, vol. 6, July 2012.
- [5] P. Calvo-Marzal, S. Sattayasamitsathit, S. Balasubramanian, J. R. Windmiller, C. Dao, J. Wang, "Propulsion of nanowire diodes" *Chemical Communications*, vol. 46 , pp. 1623-1624, 2010.

- [6] J. Wang and W. Gao, "Nano/Microscale Motors: Biomedical Opportunities and Challenges," *ACS Nano*, vol. 6, no. 7, pp. 5745-5751, July 2012.
- [7] I. S. M. Khalil, J. D. Keuning, L. Abelmann, and S. Misra, "Wireless magnetic-based control of paramagnetic microparticles," in *Proceedings of the IEEE RAS/EMBS International Conference on Biomedical Robotics and Biomechatronics (BioRob)*, pp. 460-466, Rome, Italy, June 2012.
- [8] R. Dreyfus, J. Baudry, M. L. Roper, M. Fermigier, H. A. Stone, J. Bibette, "Microscopic artificial swimmers", *Nature*, vol. 437, October 2005.
- [9] C. Pawashe, S. Floyd and M. Sitti, "Modeling and experimental characterization of an untethered magnetic micro-robot", *The International Journal of Robotics Research*, July 2009.
- [10] S. Floyd, C. Pawashe, and M. Sitti, "Microparticle manipulation using multiple untethered magnetic micro-robots on an electrostatic surface" *IEEE International Conference on Intelligent Robots and Systems*, pp. 528-533, St. Louis, USA, October 2009.
- [11] E. B. Steager, M. S. Sakar, C. Magee, M. Kennedy, A. Cowley, V. Kumar, "Automated biomanipulation of single cells using magnetic micro-robots." *The International Journal of Robotics Research*, vol. 32, pp. 346-359, March 2013.
- [12] B. J. Nelson, I. K. Kaliakatsos, and J. J. Abbott, "Microrobots for minimally invasive medicine," *Annual Review of Biomedical Engineering*, vol. 12, pp. 55-85, April 2010.

- [13] A. Ghosh and P. Fischer, "Controlled Propulsion of Artificial Magnetic Nanostructured Propellers", *Nano Letters*, vol. 9, No.6, pp. 2243-2245, April 2009.
- [14] Z. Ye, S. Regnier, and M. Sitti, "Rotating magnetic miniature swimming robots with multile flexible flagella", *IEEE Transactions on Robotics*, vol. 30, no. 1, pp. 1552-3098, February 2014.
- [15] E. Diller, J. Giltinan, and Metin Sitti, "Independent control of multiple magnetic microrobots in three dimensions" *The International Journal of Robotics Research*, vol. 32, pp. 614-631, May 2013.
- [16] S. Martel, C. C. Tremblay, S. Ngakeng, and G. Langlois, "Controlled manipulation and actuation of micro-objects with magnetotactic bacteria," *Applied Physics Letters*, vol. 89, no. 23, pp. 1-3, 2006.
- [17] S. Martel, M. Mohammadi, O Felfoul, Z. Lu, and P. Pouponneau, "Flagellated magnetotactic bacteria as controlled MRI-trackable propulsion and steering systems for medical nanorobots operating in the human microvasculature," *The International Journal of Robotics Research* vol. 28, no. 4, pp. 571-582, April 2009.
- [18] I. S. M. Khalil, M. P. Pichel, L. Abelmann, and S. Misra, Closed-loop control of magnetotactic bacteria, *The International Journal of Robotics Research*, vol. 32, no. 6, pp. 637-649, May 2013.

- 
- [19] A. A. Julius, M. S. Sakar, E. Steager, U. Cheang, M. Kim, V. Kumar, and G. J. Pappas, "Harnessing Bacterial Power in Microscale Actuation", *IEEE International Conference of Robotics and Automation (ICRA)*, Kobe, Japan, May 2009.
- [20] S. martel, O. Felfoul, J. Mathieu, A. Chanu, S. Tamaz, M. Mohammadi, M. Mankiewicz, and N. Tabatabaei, "MRI-based medical nanorobotic platform for the control of magnetic nanoparticles and flagellated bacteria for target interventions in human capillaries", *International Journal of Robotics Research*, vol. 28, no. 9, pp. 1169-1182, September 2009.
- [21] M. S. Sakar, E. B. Steager, D. H. Kim, A. A. Julius, M. Kim, V. Kumar, and G. J. Pappas, "Modeling, control and experimental characterization of microbiorobots," *International Journal of Robotics Research*, vol. 30, no. 6, pp. 647-658, May 2011.
- [22] A. A. Solovev, Y. F. Mei, E. B. Urena, G. Huang, and O. G. Schmidt, "Catalytic microtubular jet engines self-propelled by accumulated gas bubbles," *Small*, vol. 5, no. 14, pp. 1688-1692, April 2009.
- [23] A. A. Solovev, S. Sanchez, M. Pumera, Y. F. Mei, and O. G. Schmidt, "Magnetic control of tubular catalytic microbots for the transport, assembly, and delivery of micro-objects", *Advanced Functional Materials*, vol. 20, pp. 2430-2435, June 2010.
- [24] S. Sanchez, A. A. Solovev, S. M. Harazim, and Oliver G. Schmidt, "Microbots swimming in the flowing streams of microfluidic channels", *Journal of the American Chemical Society*, vol. 133, pp. 701-703, December 2010.

- 
- [25] J. G. Gibbs and Y.-P. Zhao, "Autonomously motile catalytic nanomotors" *Applied Physics Letters*, vol. 94, no. 163104, pp. 1-3, April 2009.
- [26] Y. Mei, A. A. Solovev, S. Sanchez, and O. G. Schmidt, "Rolled-up nanotech on polymers: from basic perception to self-propelled catalytic microengines", *Chemical Society Reviews*, vol. 40, no. 5, pp. 2041-3052, May 2011.
- [27] Y. Mei, G. Huang, A. A. Solovev, E. B. Urena, I. Monch, F. Ding, T. Reindl, R. K. Y. Fu, P. K. Chu, and O. G. Schmidt, "Versatile approach for integrative and functionalized tubes by strain engineering of nanomembranes on polymers", *Advanced Materials*, vol. 20, pp. 4085-4090, June 2008.
- [28] O. G. Schmidt and K. Eberl, "Thin solid films roll up into nanotubes", *Nature*, vol. 410, pp. 168, March 2001.
- [29] S. Fournier-Bidoz, A. C. Arsenault, I. Manners, and G. A. Ozin, Synthetic self-propelled nanorotors, *Chemical Communication*, vol. 441, pp. 441-443, November 2004.
- [30] A. A. Solovev, W. Xi, D. H. Gracias, S. M. Harazim, C. Deneke, S. Sanchez, and O. G. Schmidt, "Self-propelled nanotools", *AcsNano*, vol. 6, no. 2, pp. 1751-1756, January 2012.
- [31] W. F. Paxton, K. C. Kistler, C. C. Olmeda, A. Sen, S. K. St. Angelo, Y. Cao, T. E. Mallouk, P. E. Lamment, and V. H. Crespi, "Catalytic nanomotors: autonomous movement of striped nanorods", *Journal of the*

- 
- American Chemical Society*, vol. 126, no. 41, pp. 13424-13431, September 2004.
- [32] I. S. M. Khalil, H. C. Dijkslag, L. Abelman, and S. Misra, MagnetoSperm: A microrobot that navigates using weak magnetic fields, *Applied Physics Letters*, 104, 223701, June 2014.
- [33] I. S. M. Khalil, K. Youakim, A. Sanchez, and S. Misra Magnetic-based motion control of sperm-shaped microrobots using weak oscillating magnetic fields, *IEEE International Conference of Robotics and Systems (IROS)*, pp. 4686-4691, Chicago, USA, September 2014.
- [34] T. H. Boyer, "The force on a magnetic dipole," *American Journal of Physics*, vol, 56, no.8, pp. 688-692, August 1988.
- [35] S. S. Shevkoplyas, A. C. Siegel, R. M. Westervelt, M. G. Prentiss, and G. M. Whitesides, "The force acting on a superparamagnetic bead due to an applied magnetic field," *Lab on a Chip*, vol.7, no. 6, pp. 1294-1302, July 2007.
- [36] T. J. Ui, R. G. Hussey, and R. P. Roger, "Stokes drag on a cylinder in axial motion", *Physics of Fluids* vol. 27, no. 9, pp. 2381, September 1984.
- [37] S. Schuerle, S. Erni, M. Flink, B. E. Kratochvil, and B. J. Nelson, "Three-dimensional magnetic manipulation of micro- and nanostructures for applications in life sciences" *IEEE Transactions on Magnetics* vol. 49, no. 1, January 2013.

- [38] B. E. Kratochvil, M. P. Kummer, S. Erni, R. Borer, D. R. Frutiger, S. Schurle, and B. J. Nelson, MiniMag: a hemispherical electromagnetic system for 5-DOF wireless micromanipulation, *Proceeding of the 12th International Symposium on Experimental Robotics*, New Delhi, India, December 2010.
- [39] K. E. Peyer, L. Zhang, B. J. Nelson, Bio-inspired magnetic swimming microrobots for biomedical application, *Nanoscale*, vol. 5, no. 4, pp. 1259-1272, November 2012.
- [40] K. Youakim, M. Ehab, O. Hatem, S. Misra, and I. S. M. Khalil, "Paramagnetic microparticles sliding on a surface: characterization and closed-loop motion control." *IEEE International Conference of Robotics and Automation (ICRA)*, pp. 4068-4073, Seattle, USA, May 2015.